Adaptive Detection Schemes for Multistatic/Polarimetric Radar Networks

AUGUSTO AUBRY, Senior Member, IEEE
VINCENZO CAROTENUTO, Senior Member, IEEE
ANTONIO DE MAIO, Fellow, IEEE
Università degli Studi di Napoli “Federico II”, Napoli, Italy
National Inter-University Consortium for Telecommunications (CNIT), Parma, Italy

LUCA PALLOTTA, Senior Member, IEEE
University of Basilicata, Potenza, Italy

This article addresses the design of bespoke adaptive detectors for point-like targets embedded in a sea-clutter-dominated environment using a multistatic/polarimetric radar network. The system consists of one monostatic as well as two colocated and cross-polarized bistatic sensors. The detector design accounts for possible range domain heterogeneity in sea-clutter backscattering, as well as potential functional relationships between the covariance matrices that characterize clutter returns across the bistatic polarimetric nodes. Accordingly, suitable estimates of the nuisance parameters for both monostatic and bistatic measurements are employed to develop adaptive decision rules based on the two-step generalized likelihood ratio test design criterion. The performance of the proposed receivers is assessed using simultaneously recorded monostatic and cross-polarized bistatic returns collected with the netted radar system. The analysis assesses both the constant false alarm rate (CFAR) behavior and the detection capability. The results show that despite minor deviations from ideal CFAR behavior when near-zero Doppler cells are tested, all the proposed decision rules maintain an overall robust CFAR behavior with respect to the nuisance parameters. In terms of detection capability, the proposed strategies outperform those relying solely on monostatic measurements and demonstrate comparable, or slightly improved, performance with respect to a competing approach confirming the effectiveness and robustness of the devised techniques.

I. INTRODUCTION

Multistatic/polarimetric radars are sensing systems that exploit both spatial and polarimetric diversity to improve the performance of conventional monostatic and bistatic configurations. However, the design of reliable coherent detection schemes that fully integrate the information collected by such systems remains challenging, particularly when targets are embedded in cluttered environments [1].

In multistatic/polarimetric systems, spatial and polarimetric diversity can lead to diversifications in the statistical properties of the clutter perceived at each node of the network, a phenomenon known as clutter diversity [2], [3], [4], [5]. If such variations are correctly accounted for at the detector design stage, then they can be effectively exploited to enhance target detectability, particularly in challenging environments where conventional single-node or single-polarization systems may fail [6], [7], [8], [9], [10], [11], [12], [13], [14].

To accurately characterize clutter diversity, it is crucial leveraging measured data, as they provide the empirical foundation necessary to capture the statistical variability and features of such a disturbance. In this respect, over the past few years, measurements collected using the Netted RADar (NetRAD) system [15] have been analyzed to glean relevant bistatic and multistatic sea-clutter characteristics [15], [16], [17], [18], [19], [20], [21], [22], [23], [24], [25], [26], [27], [28], [29], [30], [31], [32], [33], [34]. Among these, in [33], a statistical analysis of simultaneously collected monostatic and cross-polarized bistatic sea-clutter returns highlighted that the spherically invariant random process (SIRP) representation [35], [36], [37], [38], [39], [40], [41], [42] is a suitable choice for describing the sea-clutter interference environment at both monostatic and bistatic sensors. According to the SIRP model, over a suitable time interval (referred to as the coherence time), sea-clutter backscattering is modeled as the product of a nonnegative random variable (texture component) and a zero-mean circularly symmetric Gaussian process with unknown spectral characteristics (speckle component). In addition, the analysis in [33] also highlighted that the monostatic clutter data exhibited faster fluctuations over the range domain than those observed for the bistatic measurements. Exploiting the same measurements used in [33], further investigations in [34] showed that within the coherence time, the bistatic returns across different polarimetric channels can be modeled as Gaussian and statistically independent, with possibly proportional or equal covariance matrices depending on the geometric and polarimetric system configuration.

Received 17 June 2025; revised 6 October 2025 and 8 January 2026; accepted 14 January 2026. Date of publication 19 January 2026; date of current version 30 March 2026.

DOI. No. 10.1109/TAES.2026.3655255

Refereeing of this contribution was handled by M. Ritchie.

The work of Augusto Aubry, Vincenzo Carotenuto, and Antonio De Maio was supported by European Union under the Italian National Recovery and Resilience Plan (NRRP) of NextGenerationEU, partnership on “Telecommunications of the Future” through project “RESTART” under Grant PE00000001.

Authors’ addresses: Augusto Aubry, Vincenzo Carotenuto, and Antonio De Maio are with the Department of Electrical Engineering and Information Technology (DIETI), Università degli Studi di Napoli “Federico II,” 80125 Napoli, Italy, and also with National Inter-University Consortium for Telecommunications (CNIT), 43124 Parma, Italy, E-mail: (augusto.aubry@unina.it; vincenzo.carotenuto@unina.it; ademaio@unina.it); Luca Pallotta is with the Department of Engineering (DiING), University of Basilicata, 85100 Potenza, Italy, E-mail: (luca.pallotta@unibas.it). *(Corresponding author: Antonio De Maio.)*

In this article, the statistical insights gained in [33] and [34] are capitalized to design adaptive detection schemes for point-like targets embedded in sea-clutter-dominated environments, with reference to a multistatic/polarimetric radar system composed of one monostatic and two colocated, cross-polarized bistatic sensors. Specifically, adaptive decision rules are synthesized jointly exploiting both monostatic and bistatic measurements. To this end, both potential range domain heterogeneity and possible functional relationships among the covariance structures at the different nodes are appropriately accounted for. In this respect, suitable estimates of the nuisance parameters are capitalized to develop decision architectures relying on the two-step generalized likelihood ratio test (GLRT) criterion [43]. Therefore, three polarimetric adaptive receivers are proposed (based on the type of functional dependence between the clutter covariance matrices at the bistatic nodes), denoted as polarimetric homogeneous detector (pol-HO), polarimetric partially homogeneous detector (pol-PH), and polarimetric heterogeneous detector (pol-HE).

At the analysis stage, simultaneously recorded monostatic and cross-polarized bistatic sea-clutter data, collected via the NetRAD system, are exploited to investigate both the constant false alarm rate (CFAR) behavior and the detection capability of the conceived decision rules. The former aims at establishing the ability of the proposed detection schemes to achieve a desired false alarm probability (P_{fa}) that remains constant regardless of the nuisance parameters values. The latter assesses the detection probability (P_d) by synthetically injecting a target representative of a small boat into the available target-free clutter data, with its response, in particular the radar cross section (RCS) values, synthesized leveraging the MATLAB POFacets toolbox [44], [45].

The results show that although some deviations from the ideal CFAR behavior are observed as near-zero Doppler cells are tested, the proposed strategies maintain an overall robust CFAR behavior. In particular, the pol-HO exhibits the largest deviations from ideal CFAR behavior when vertical–horizontal (VH) polarizations are used for transmission-reception at the monostatic node. In contrast, with horizontal-horizontal (HH) polarization at the monostatic node, it performs similarly to the pol-PH. The pol-HE delivers the best CFAR performance across all considered datasets, regardless of the polarimetric configuration, and also outperforms a competing receiver from the open literature [29], [46], [47], [48] that leverages multistatic and polarimetric data. Regarding the P_d analysis, the homogeneous (HO) and partially homogeneous (PH) architectures exhibit similar performance, with the latter slightly outperforming the former. Consistently with the CFAR analysis, the pol-HE provides the best detection performance across all considered scenarios, surmounting the competing approach. Notably, the analysis also highlights that using horizontal polarization at the transmit side leads to higher P_d values than vertical polarization. This outcome is expected, since, as observed in [33], the clutter power perceived at both cross-polarized bistatic channels when vertical polarization is used at the transmit side is higher than the setup with horizontal transmission, a trend that aligns with empirical evidence observed in conventional monostatic sea-clutter data. Not surprisingly, it can be observed that target velocity vectors state affects the P_d curves. Indeed, if both monostatic and bistatic Doppler shifts lie outside the respective clutter spectra, the target just competes with background noise.

The main contributions of this work can be summarized as follows.

1) Design of novel adaptive detection architectures for point-like targets in sea clutter, jointly leveraging both monostatic and cross-polarized bistatic radar returns. The proposed decision rules account for both range domain heterogeneity at the monostatic sensor and possible functional relationships among the clutter covariance matrices across bistatic nodes.
2) Development of three polarimetric detectors (namely, pol-HO, pol-PH, and pol-HE), each derived under different assumptions on the relationship between the clutter covariance matrices at the bistatic sensors.
3) Performance assessment using measured sea-clutter NetRAD data, analyzing CFAR behavior under various polarimetric settings, as well as detection capability using synthetic boat targets generated via the MATLAB POFacets toolbox.

The rest of this article is organized as follows. Section II focuses on the synthesis of adaptive detection schemes that jointly utilize both monostatic and cross-polarized bistatic measurements. Section III gives a brief overview of the NetRAD system and the considered data, followed by the performance assessment of the synthesized detectors. Finally, Section IV presents the conclusions and discusses possible avenues for future research.

Notations: Boldface is used for vectors $\boldsymbol{a}$ (lower case) and matrices $\boldsymbol{a}$ (upper case). The conjugate, transpose, and conjugate transpose operators are denoted by the symbols $(\cdot)^*$, $(\cdot)^T$, and $(\cdot)^\dagger$, respectively, whereas the symbol $(\cdot)^{-1}$ indicates the inverse. $\text{tr}\{\cdot\}$ and $\det\{\cdot\}$ are the trace and the determinant of their square matrix argument. $\mathbb{R}^N$, $\mathbb{C}^N$, $\mathbb{R}^{N\times M}$, and $\mathbb{C}^{N\times M}$ are the set of N-dimensional vectors of real numbers, complex numbers, $N\times M$ real matrices, and $N\times M$ complex matrices, respectively. The letter j represents the imaginary unit (i.e., $j=\sqrt{-1}$), and for any complex number x, $|x|$ represents the modulus of x. Moreover, $\mathbb{E}[\cdot]$ denotes statistical expectation. Finally, $\boldsymbol{x}\sim\mathcal{CN}(\boldsymbol{\mu},\boldsymbol{M})$ means that $\boldsymbol{x}$ is a complex circularly symmetric Gaussian random vector with mean vector $\boldsymbol{\mu}$ and covariance matrix $\boldsymbol{M}$, whereas $\varphi\sim\mathcal{U}[0,2\pi]$ indicates that φ is a uniform random variable within the interval $[0,2\pi]$.

II. PROBLEM FORMULATION AND DETECTORS DESIGN

Let us consider a multistatic/polarimetric radar system operating in a sea-clutter environment, composed of two

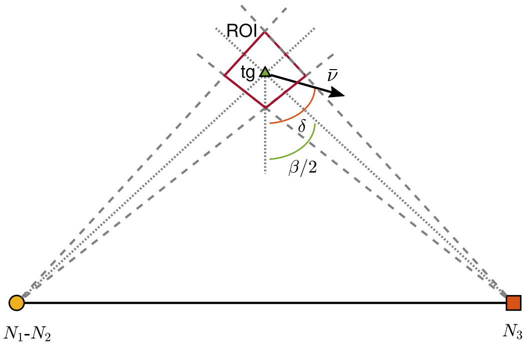

Fig. 1. Geometric configuration of the considered multistatic/polarimetric radar system.

colocated, cross-polarized bistatic sensors and one monostatic node, referred to as N_1, N_2, and N_3, respectively. Nodes N_1 and N_2 are equipped with horizontally and vertically polarized receiving antennas, respectively, both steered in the same direction. Node N_3, on the other hand, is equipped with separate transmit and receive antennas, enabling the reception of either copolarized or cross-polarized radar returns, depending on the adopted polarimetric configuration (namely, HH, HV, VH, or vertical-vertical (VV)).

As depicted in Fig. 1, all antennas are steered toward a common region of interest (ROI), whose center corresponds to the intersection of their steering directions. This point, together with the node locations, forms the vertices of an isosceles triangle, whose axis of symmetry is perpendicular to the bistatic baseline. The extent of the ROI is determined by the antennas' beamwidth, which, along with the gains, is assumed the same across all nodes.

It is worth noting that while this sensing system setup is specific to a particular surveillance configuration, it matches the deployment used for the NetRAD system, enabling performance assessment of the designed detectors on measured data. Nonetheless, the developed framework can be readily extended to accommodate a more general sensing geometry.

With reference to the considered system setup, assume that N_3 transmits a burst of N pulses with a given Pulse Repetition Time (PRT). Thus, for a specific cell under test (CUT), the problem of detecting a target embedded in a sea-clutter-dominated environment by jointly using both monostatic and bistatic measurements can be formulated in terms of the following binary hypothesis test:

$$\begin{cases} \mathcal{H}_0: \begin{cases} \boldsymbol{z}_i = \boldsymbol{n}_i, & i = 1, 2, 3 \\ \boldsymbol{z}_{i,k} = \boldsymbol{n}_{i,k}, & i = 1, 2, 3, \quad k = 1, \dots, K \end{cases} \\ \\ \mathcal{H}_1: \begin{cases} \boldsymbol{z}_i = \alpha_i \boldsymbol{s}_i + \boldsymbol{n}_i, & i = 1, 2, 3 \\ \boldsymbol{z}_{i,k} = \boldsymbol{n}_{i,k}, & i = 1, 2, 3, \quad k = 1, \dots, K \end{cases} \end{cases} \tag{1}$$

where

1) $\boldsymbol{z}_i \in \mathbb{C}^N$, $i = 1, 2, 3$, is the N-dimensional observation vector (referred to as primary data), whose entries are the slow-time samples collected from the CUT at the ith node;
2) $\boldsymbol{z}_{i,k} \in \mathbb{C}^N$, $i = 1, 2, 3$, $k = 1, \dots, K$, is a set of $K \geq N$ independent observation vectors (referred to as secondary data) available at the ith node that are (ideally) free of the prospective target contribution and share the same disturbance covariance structure as the primary data;
3) $\alpha_i \in \mathbb{C}$, $i = 1, 2, 3$, is an unknown parameter that accounts for both the RCS of the target and the channel propagation effects at the ith node;
4) $\boldsymbol{s}_i \in \mathbb{C}^N$ is the temporal steering vector defined as
$$\boldsymbol{s}_i = \left[1, e^{j2\pi \upsilon_{D_i}}, \dots, e^{j2\pi(N-1)\upsilon_{D_i}}\right]^T, \; i = 1, 2, 3$$
with υ_{D_i} being the normalized target Doppler frequency experienced at the ith node;
5) $\boldsymbol{n}_i \in \mathbb{C}^N$ and $\boldsymbol{n}_{i,k} \in \mathbb{C}^N$, $i = 1, 2, 3$, $k = 1, \dots, K$, are data vectors containing the slow-time interference samples for the primary and secondary data, respectively.

Assuming the target located at the center of the ROI and considering the geometry depicted in Fig. 1, the bistatic and monostatic normalized Doppler frequencies can be expressed as [49, Ch. 6, pp. 119–120]

$$\upsilon_{D_1} = \upsilon_{D_2} = \frac{2v_0}{\lambda} \cos(\delta) \cos(\beta/2) \cdot T_{\text{PRT}} \tag{2}$$

$$\upsilon_{D_3} = \frac{2v_0}{\lambda} \cos(\delta - \beta/2) \cdot T_{\text{PRT}} \tag{3}$$

where β is the bistatic angle, δ is the aspect angle of the target velocity vector with respect to the bistatic bisector, T_{PRT} is the PRT, and v_0 is the actual modulus of target velocity vector.

As to the statistical characterization of the disturbance contribution, analyses conducted in [33] and [34] on monostatic and cross-polarized bistatic sea-clutter returns, simultaneously collected via the NetRAD system, revealed the following.

1) Both monostatic and bistatic sea-clutter returns can be modeled according to an SIRP representation, namely, as the product of a nonnegative random variable (texture component) and a zero-mean circularly symmetric Gaussian process with unknown spectral characteristics (speckle component).
2) Regardless of the bistatic angle and polarization used at the transmission side, monostatic data exhibited faster fluctuations over the range domain than those observed in the bistatic measurements.
3) Within the coherence time, bistatic returns across the two polarimetric channels can be modeled as statistically independent Gaussian vectors, with covariance matrices that may be proportional or equal, depending on the bistatic angle and the polarization used at the transmission side.
4) For both monostatic and bistatic data, the coherence time is on the order of seconds, which is significantly longer than the typical coherent processing interval (CPI) intervals used for radar detection.

Leveraging the previous insights and assuming a CPI that is shorter than the coherence time, as well as modeling the texture as an unknown deterministic parameter, the radar returns from different range cells at the monostatic node can be modeled as zero-mean, circularly symmetric complex Gaussian vectors, sharing the same covariance matrix structure but exhibiting different unknown scaling factors. In contrast, echoes collected via the bistatic sensors from different range cells can be assumed to be zero-mean, circularly symmetric complex Gaussian vectors, sharing the same sensor-specific covariance matrix (which can be equal, proportional, or distinct, depending on the geometric and polarimetric configuration between the bistatic nodes of the system). Following these guidelines, the disturbance contributions perceived at the bistatic and monostatic nodes can be modeled as

$$N_1 : \begin{cases} \boldsymbol{n}_1 \sim \mathcal{CN}(0, \boldsymbol{M}_1) \\ \boldsymbol{n}_{1,k} \sim \mathcal{CN}(0, \boldsymbol{M}_1), \quad k = 1, \ldots, K \end{cases}$$
$$N_2 : \begin{cases} \boldsymbol{n}_2 \sim \mathcal{CN}(0, \boldsymbol{M}_2) \\ \boldsymbol{n}_{2,k} \sim \mathcal{CN}(0, \boldsymbol{M}_2), \quad k = 1, \ldots, K \end{cases}$$
$$N_3 : \begin{cases} \boldsymbol{n}_3 \sim \mathcal{CN}(0, \sigma \boldsymbol{R}_3) \\ \boldsymbol{n}_{3,k} \sim \mathcal{CN}(0, \sigma_k \boldsymbol{R}_3), \quad k = 1, \ldots, K \end{cases} \tag{4}$$

where σ and $\sigma_k, k = 1, \ldots, K$, are unknown positive scaling factors accounting for the heterogeneity of the monostatic data along the range domain.[1] In addition, based on previous observations regarding the possible relationships between the covariance matrices of the bistatic measurements [34], the following three radar scenarios are considered:

$$\begin{cases} \boldsymbol{M}_1 = \boldsymbol{M}_2, & \text{homogeneous case} \\ \boldsymbol{M}_1 = \gamma \boldsymbol{M}_2, & \text{partially homogeneous case} \\ \boldsymbol{M}_1 \neq \boldsymbol{M}_2, & \text{heterogeneous case} \end{cases} \tag{5}$$

with $\gamma > 0$. Leveraging the assumptions in (4), the probability density function (pdf) of the primary and secondary data under the null and alternative hypotheses, $\mathcal{H}_\ell, \ell = 0, 1$, can be written, respectively, as

$$f(\boldsymbol{z}_i | \ell\alpha_i, \boldsymbol{M}_i, \mathcal{H}_\ell) = \frac{1}{\pi^N \det(\boldsymbol{M}_i)} \times \exp\left[-(\boldsymbol{z}_i - \ell\alpha_i \boldsymbol{s}_i)^\dagger \boldsymbol{M}_i^{-1} (\boldsymbol{z}_i - \ell\alpha_i \boldsymbol{s}_i)\right], \ i = 1, 2$$
$$f(\boldsymbol{z}_3 | \ell\alpha_3, \sigma, \boldsymbol{R}_3, \mathcal{H}_\ell) = \frac{1}{\pi^N \sigma^N \det(\boldsymbol{R}_3)} \times \exp\left[-\frac{(\boldsymbol{z}_3 - \ell\alpha_3 \boldsymbol{s}_3)^\dagger \boldsymbol{R}_3^{-1} (\boldsymbol{z}_3 - \ell\alpha_3 \boldsymbol{s}_3)}{\sigma}\right] \tag{6}$$

and

$$f\left(\boldsymbol{z}_{i,1}, \ldots, \boldsymbol{z}_{i,K} | \ell\alpha_i, \boldsymbol{M}_i, \mathcal{H}_\ell\right) = \frac{1}{\pi^{NK} (\det(\boldsymbol{M}_i))^K} \times \exp\left\{\sum_{k=1}^{K} \left[-\left(\boldsymbol{z}_{i,k} - \ell\alpha_i \boldsymbol{s}_i\right)^\dagger \boldsymbol{M}_i^{-1} \left(\boldsymbol{z}_{i,k} - \ell\alpha_i \boldsymbol{s}_i\right)\right]\right\},$$
$$i = 1, 2$$
$$f\left(\boldsymbol{z}_{3,1}, \ldots, \boldsymbol{z}_{3,K} | \ell\alpha_3, \boldsymbol{R}_3, \sigma_1, \ldots, \sigma_K, \mathcal{H}_\ell\right) = \frac{1}{\pi^{NK} \prod_{k=1}^{K} \sigma_k^N \det(\boldsymbol{R}_3)} \times \exp\left\{\sum_{k=1}^{K} \left[-\frac{\left(\boldsymbol{z}_{3,k} - \ell\alpha_3 \boldsymbol{s}_3\right)^\dagger \boldsymbol{R}_3^{-1} \left(\boldsymbol{z}_{3,k} - \ell\alpha_3 \boldsymbol{s}_3\right)}{\sigma_k}\right]\right\}. \tag{7}$$

The optimal solution to the hypothesis testing problem in (1) (in the Neyman–Pearson sense) is the likelihood ratio test (LRT), which is given by

$$\frac{f(\boldsymbol{z}_1, \boldsymbol{z}_2, \boldsymbol{z}_3 | \alpha_1, \alpha_2, \alpha_3, \sigma, \boldsymbol{M}_1, \boldsymbol{M}_2, \boldsymbol{R}_3, \mathcal{H}_1)}{f(\boldsymbol{z}_1, \boldsymbol{z}_2, \boldsymbol{z}_3 | \sigma, \boldsymbol{M}_1, \boldsymbol{M}_2, \boldsymbol{R}_3, \mathcal{H}_0)} \underset{\mathcal{H}_0}{\overset{\mathcal{H}_1}{\gtrless}} \eta \tag{8}$$

where $f(\boldsymbol{z}_1, \boldsymbol{z}_2, \boldsymbol{z}_3 | \cdot)$ is the joint pdf of the bistatic and monostatic measurements, and η is the detection threshold set to ensure the desired P_{fa}. Notably, the practical implementation of the LRT is precluded since it requires knowledge of the target scattering parameters $\alpha_i, i = 1, 2, 3$, as well as the data covariance matrices $\boldsymbol{M}_i, i = 1, 2, \boldsymbol{R}_3$, and the power scaling factor σ. Thus, to develop a practically implementable detector, the two-step GLRT criterion is pursued [43]. Specifically, the decision rule is designed by first computing the GLRT assuming that $\boldsymbol{M}_i, i = 1, 2$, and $\boldsymbol{R}_3$ are known (step 1), and then replacing these matrices in the resulting test with suitable estimates (step 2).

According to the first step, leveraging the statistical independence of the measurements collected at each node, the GLRT for known $\boldsymbol{M}_i, i = 1, 2$, and $\boldsymbol{R}_3$ is given by

$$\frac{\max\limits_{\alpha_i, \sigma} f_{\boldsymbol{z}_3}(\boldsymbol{z}_3 | \alpha_3, \sigma, \boldsymbol{R}_3, \mathcal{H}_1) \prod_{i=1}^{2} f_{\boldsymbol{z}_i}(\boldsymbol{z}_i | \alpha_i, \boldsymbol{M}_i, \mathcal{H}_1)}{\max\limits_{\sigma} f_{\boldsymbol{z}_3}(\boldsymbol{z}_3 | \sigma, \boldsymbol{R}_3, \mathcal{H}_0) \prod_{i=1}^{2} f_{\boldsymbol{z}_i}(\boldsymbol{z}_i | \boldsymbol{M}_i, \mathcal{H}_0)} \underset{\mathcal{H}_0}{\overset{\mathcal{H}_1}{\gtrless}} \eta. \tag{9}$$

It is not difficult to prove that the previous decision rule is statistically equivalent to

$$g(\boldsymbol{s}_1, \boldsymbol{s}_2, \boldsymbol{s}_3, \boldsymbol{z}_1, \boldsymbol{z}_2, \boldsymbol{z}_3, \boldsymbol{M}_1, \boldsymbol{M}_2, \boldsymbol{R}_3) = \sum_{i=1}^{2} g_i(\boldsymbol{s}_i, \boldsymbol{z}_i, \boldsymbol{M}_i) - N \log\left[g_3(\boldsymbol{s}_3, \boldsymbol{z}_3, \boldsymbol{R}_3)\right] \underset{\mathcal{H}_0}{\overset{\mathcal{H}_1}{\gtrless}} \xi \tag{10}$$

where ξ is the modified detection threshold, whereas the statistics $g_i(\cdot), i = 1, 2, 3$, are given by

$$g_i(\boldsymbol{s}_i, \boldsymbol{z}_i, \boldsymbol{M}_i) = \frac{\left|\boldsymbol{s}_i^\dagger \boldsymbol{M}_i^{-1} \boldsymbol{z}_i\right|^2}{\boldsymbol{s}_i^\dagger \boldsymbol{M}_i^{-1} \boldsymbol{s}_i}, \quad i = 1, 2$$
$$g_3(\boldsymbol{s}_3, \boldsymbol{z}_3, \boldsymbol{R}_3) = 1 - \frac{\left|\boldsymbol{s}_3^\dagger \boldsymbol{R}_3^{-1} \boldsymbol{z}_3\right|^2}{\left(\boldsymbol{s}_3^\dagger \boldsymbol{R}_3^{-1} \boldsymbol{s}_3\right)\left(\boldsymbol{z}_3^\dagger \boldsymbol{R}_3^{-1} \boldsymbol{z}_3\right)}. \tag{11}$$

---

[1] Notice that the covariance matrix of the primary data is $\boldsymbol{M}_3 = \sigma \boldsymbol{R}_3$. Thus, $\boldsymbol{R}_3$ contains covariance structure information common to both primary and secondary data.

To develop a fully adaptive decision rule, in line with step 2, suitable estimates $\hat{\boldsymbol{M}}_1$, $\hat{\boldsymbol{M}}_2$, and $\hat{\boldsymbol{R}}_3$ of the true covariance matrices are plugged into (10), leading to

$$g(\boldsymbol{s}_1, \boldsymbol{s}_2, \boldsymbol{s}_3, z_1, z_2, z_3, \hat{\boldsymbol{M}}_1, \hat{\boldsymbol{M}}_2, \hat{\boldsymbol{R}}_3) \overset{\mathcal{H}_1}{\underset{\mathcal{H}_0}{\gtrless}} \hat{\xi} \tag{12}$$

with $\hat{\xi}$ set to fulfill P_{fa} requirement. For both monostatic and bistatic measurements, the interference covariance matrices can be estimated using the secondary data $z_{i,k}$, $i = 1, 2, 3$, $k = 1, \ldots, K$. Specifically, according to the radar scenarios described in (5), by jointly exploiting the secondary data collected at N_1 and N_2, the covariance matrices for the HO and heterogeneous (HE) cases can be estimated as follows:

$$\hat{\boldsymbol{M}}_1^{\text{HO}} = \hat{\boldsymbol{M}}_2^{\text{HO}} = \frac{1}{2K}\sum_{k=1}^{K}\left(z_{1,k}\boldsymbol{z}_{1,k}^{\dagger} + z_{2,k}\boldsymbol{z}_{2,k}^{\dagger}\right) \tag{13}$$

$$\hat{\boldsymbol{M}}_1^{\text{HE}} = \frac{1}{K}\sum_{k=1}^{K} z_{1,k}\boldsymbol{z}_{1,k}^{\dagger}, \quad \hat{\boldsymbol{M}}_2^{\text{HE}} = \frac{1}{K}\sum_{k=1}^{K} z_{2,k}\boldsymbol{z}_{2,k}^{\dagger}. \tag{14}$$

For the PH case, suitable estimates of $\boldsymbol{M}_1$ and $\boldsymbol{M}_2$ can be obtained using the recursive procedure outlined in Algorithm 1. Finally, for the monostatic measurements, the covariance matrix $\boldsymbol{R}_3$ can be estimated following the recursive procedure, as described in Algorithm 2 [50].

Based on the previous estimates, three polarimetric adaptive detection schemes that jointly exploit both monostatic and bistatic measurements are obtained. These are referred to as pol-HO, pol-PH, and pol-HE, with their respective decision statistics given by

$$\begin{aligned}
\mathcal{T}_{\text{HO}} &= g(\boldsymbol{s}_1, \boldsymbol{s}_2, \boldsymbol{s}_3, z_1, z_2, z_3, \hat{\boldsymbol{M}}_1^{\text{HO}}, \hat{\boldsymbol{M}}_2^{\text{HO}}, \hat{\boldsymbol{R}}_3) \text{ [pol-HO]}\\
\mathcal{T}_{\text{PH}} &= g(\boldsymbol{s}_1, \boldsymbol{s}_2, \boldsymbol{s}_3, z_1, z_2, z_3, \hat{\boldsymbol{M}}_1^{\text{PH}}, \hat{\boldsymbol{M}}_2^{\text{PH}}, \hat{\boldsymbol{R}}_3) \text{ [pol-PH]}\\
\mathcal{T}_{\text{HE}} &= g(\boldsymbol{s}_1, \boldsymbol{s}_2, \boldsymbol{s}_3, z_1, z_2, z_3, \hat{\boldsymbol{M}}_1^{\text{HE}}, \hat{\boldsymbol{M}}_2^{\text{HE}}, \hat{\boldsymbol{R}}_3) \text{ [pol-HE].}
\end{aligned} \tag{15}$$

Notably, under the corresponding design assumptions, each detection scheme achieves the CFAR property with respect to the covariance matrices of both monostatic and bistatic data, as well as the texture components of the monostatic measurements. As a matter of fact, the CFAR property arises from the fact that the integrated multipolarimetric/multinode decision statistic in (10) can be expressed as the sum of independent CFAR statistics, each corresponding to the single-polarization/single-node case. Finally, it is worth noting that the computational complexity of the three proposed algorithms is primarily dictated by the estimation of the covariance matrix at the monostatic node $\boldsymbol{R}_3$, which constitutes the most computationally demanding step of the process. Specifically, it is on the order of $\mathcal{O}(Q_2 \cdot K \cdot N^2)$ (according to the Landau notation), where Q_2 is the number of iterations in Algorithm 2.

Algorithm 1: Procedure to Estimate $\boldsymbol{M}_1$ and $\boldsymbol{M}_2$ for the Bistatic Data Under the Assumption $\boldsymbol{M}_2 = \gamma\boldsymbol{M}_1$.

```
Input: $z_{1,k}, z_{2,k}, k = 1, \ldots, K$, and $Q_1$
Output: $\hat{\boldsymbol{M}}_1^{PH}, \hat{\boldsymbol{M}}_2^{PH}$
compute
    $\boldsymbol{s}_1 = \frac{1}{K}\sum_{k=1}^{K} z_{1,k}\boldsymbol{z}_{1,k}^{\dagger}, \quad \boldsymbol{s}_2 = \frac{1}{K}\sum_{k=1}^{K} z_{2,k}\boldsymbol{z}_{2,k}^{\dagger}$
set $q = 0, \boldsymbol{B}_0 = \boldsymbol{s}_1$
repeat
    $q = q + 1$
    $\kappa_q = \frac{1}{N}\text{tr}[\boldsymbol{s}_2\boldsymbol{B}_{q-1}^{-1}]$
    $\boldsymbol{B}_q = \frac{1}{2}(\boldsymbol{s}_1 + \frac{\boldsymbol{s}_2}{\kappa_q})$
until $q \leq Q_1$
set $\hat{\boldsymbol{M}}_1^{PH} = \boldsymbol{B}_q, \hat{\boldsymbol{M}}_2^{PH} = \kappa_q\boldsymbol{B}_q$
```

Algorithm 2: Procedure to Estimate $\boldsymbol{R}_3$ for the Monostatic Data.

```
Input: $z_{3,k}, k = 1, \ldots, K$, and $Q_2$
Output: $\hat{\boldsymbol{R}}_3$
set $q = 0$ and $\boldsymbol{B}_0 = \frac{N}{K}\sum_{k=1}^{K}\frac{z_{3,k}\boldsymbol{z}_{3,k}^{\dagger}}{\boldsymbol{z}_{3,k}^{\dagger}z_{3,k}}$
repeat
    $q = q + 1$
    $\boldsymbol{B}_q = \frac{N}{K}\sum_{k=1}^{K}\frac{z_{3,k}\boldsymbol{z}_{3,k}^{\dagger}}{\boldsymbol{z}_{3,k}^{\dagger}\boldsymbol{B}_{q-1}^{-1}z_{3,k}}$
until $q \leq Q_2$
set $\hat{\boldsymbol{R}}_3 = \boldsymbol{B}_q$
```

III. PERFORMANCE ANALYSIS

In this section, the performance of the devised adaptive detection schemes is assessed using monostatic and bistatic sea-clutter returns collected simultaneously via the NetRAD system. Specifically, Section III-A provides an overview of the main features of the NetRAD along with a description of the considered datasets. In Sections III-B and III-C, the capabilities of the designed detectors to guarantee the CFAR property and their detection performance are evaluated, respectively.

Moreover, the multichannel-normalized adaptive matched filter (M-NAMF) [29], [46], [47], [48] and the NAMF applied on the monostatic data (m-NAMF) are also considered as terms of comparison. In particular, the decision statistic for the M-NAMF is given by [29], [46]

$$\mathcal{T}_{\text{M-NAMF}} = \prod_{i=1}^{3}\left[1 - \frac{\left|\boldsymbol{s}_i^{\dagger}\boldsymbol{M}_i^{-1}z_i\right|^2}{\left(\boldsymbol{s}_i^{\dagger}\boldsymbol{M}_i^{-1}\boldsymbol{s}_i\right)\left(z_i^{\dagger}\boldsymbol{M}_i^{-1}z_i\right)}\right]^{-1} \tag{16}$$

whereas the expression of the m-NAMF is obtained extracting the term for $i = 3$ from (16), namely

$$\mathcal{T}_{\text{m-NAMF}} = \left[1 - \frac{\left|\boldsymbol{s}_3^{\dagger}\boldsymbol{M}_3^{-1}z_3\right|^2}{\left(\boldsymbol{s}_3^{\dagger}\boldsymbol{M}_3^{-1}\boldsymbol{s}_3\right)\left(z_3^{\dagger}\boldsymbol{M}_3^{-1}z_3\right)}\right]^{-1}. \tag{17}$$

Note that the covariance matrix $\boldsymbol{M}_i$, $i = 1, 2, 3$, involved in (16) is estimated via Algorithm 2 with input the secondary

TABLE I
Specifications of the Used NetRAD Datasets

Datasets	Pol. N_3 (Tx–Rx)	Pol. N_1 (Rx)	Pol. N_2 (Rx)	β
1	HH	H	V	60°
8	VH	H	V	
4	HH	H	V	90°
11	VH	H	V	
5	HH	H	V	95°
12	VH	H	V	

data available at the ith node, and similarly for the estimate of $\boldsymbol{M}_3$ in (17). Moreover, for all the conducted simulations, $Q_1 = 5$ and $Q_2 = 15$ are set in Algorithms 1 and 2.

A. NetRAD and Data Description

As introduced in Sections I and II, the NetRAD is a multistatic/polarimetric system, deployed as illustrated in Fig. 1, and composed of one monostatic sensor (N_3) and two coocated, cross-polarized bistatic nodes (N_1-N_2). It is an S-band ground-based system operating over a carrier frequency of 2.4 GHz, transmitting pulse trains of linear up-chirp waveforms from N_3. The considered data refer to a sensing system configuration in which the nodes N_1 and N_2 were separated from N_3 by a baseline of 1830 m. Moreover, N_3 was operated with a probing waveform with a swept bandwidth of 45 MHz (i.e., a range resolution of 3.3 m) and $T_{\mathrm{PRT}} = 1$ ms. Furthermore, as highlighted in Fig. 1, acquisitions for different bistatic angles were collected by suitably pointing the antennas of N_1, N_2, and N_3 toward a specific ROI (referred to as the clutter patch hereafter). At each node and for each bistatic angle, measurements were recorded over an acquisition time interval of 130 s, corresponding to $N_s = 130\,000$ slow-time samples for each range cell.[2] Finally, regarding the environmental conditions, the wind speed was about 8–9 m/s, while the wave height was approximately 2 m (sea state 4), and both remained almost constant during the measurement campaign. For more details on the geometric and polarimetric system configuration, refer to [33] and [34].

Table I presents an overview of the polarization setups for each dataset considered in this analysis.

It should be noted that in cases where measured data are not available, physics-based channel simulation tools (such as RFView developed by ISL [52]) offer realistic clutter models that can support the evaluation of detection algorithms [52], [53], [54], [55].

B. CFAR Analysis

The CFAR property ensures that the detection threshold can be set to guarantee a preassigned P_{fa}, independently of the actual disturbance parameters. According to the design assumptions and considering both primary and secondary data, the nuisance parameters include σ, σ_k $(k = 1, \ldots, K)$, $\boldsymbol{R}_3$ for the monostatic returns, and $\boldsymbol{M}_i$ $(i = 1, 2)$ for the bistatic measurements.

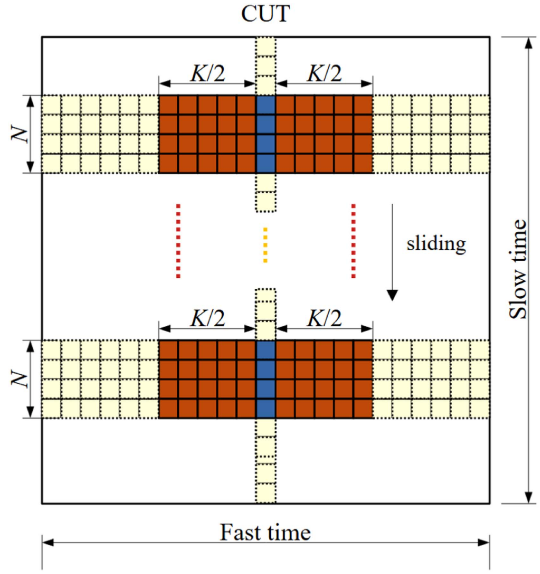

Fig. 2. Pictorial representation of the data selection procedure.

To account for correlations among the fast-time samples of both monostatic and bistatic data, which is closely related to the sea swell or sea wave patterns [8], the detection thresholds for each technique (viz., pol-HO, pol-PH, and pol-HE) have been set under the assumption of colored Gaussian clutter. Precisely, the primary and secondary data $\boldsymbol{z}_i$ and $\boldsymbol{z}_{i,k}$, $i = 1, 2, 3$, $k = 1, \ldots, K$, have been modeled as identically distributed zero-mean circularly symmetric complex Gaussian random vectors characterized by a fast-time correlation matrix $\boldsymbol{C}_i$, $i = 1, 2, 3$. For each case study, $\boldsymbol{C}_i$ is estimated as a Hermitian Toeplitz matrix, whose first row contains the first $K + 1$ samples of the fast-time correlation (estimated averaging multiple realizations in the slow-time domain) of the measurements collected via the node N_i, $i = 1, 2, 3$, respectively. Accordingly, the detection thresholds have been set using Monte Carlo counting techniques based on $100/P_{\mathrm{fa}}$ independent trials, assuming $N = 8$ and $K = 16$, to ensure, for each detection scheme, a nominal $P_{\mathrm{fa}} = 10^{-2}$ for zero-velocity.

Regarding the actual P_{fa}, it has been estimated using the available measurements by considering, for each sensor, the radar echoes from the center of the clutter patch (i.e., the selected "blue" CUT) as primary data, and those from $K = 16$ range cells spatially close to the CUT as secondary data, selected as $K/2$ on the left and $K/2$ on the right. More precisely, based on the pictorial representation in Fig. 2, for both monostatic and bistatic sensors, at each range, the 130000 available slow-time samples have been partitioned into disjoint vectors of $N = 8$ samples (without overlap), forming multiple instances of primary and secondary data.

Exploiting this data selection procedure, and considering two case studies with reference to the velocity direction ruling the design steering vectors, the actual P_{fa} of each

---

[2] It is worth noting that since the PRT used to collect the data is 1 ms, the CPI for the considered value of N is on the order of a few milliseconds. This duration is significantly shorter than both the total data acquisition time (130 s) and the estimated decorrelation time of the data (approximately 50 ms, as reported in [34] and consistent with the values in [51]).

detection scheme has been estimated as the fraction of instances in which the decision statistic exceeds the corresponding detection threshold.[3] Specifically, the analysis has been conducted by setting $\delta = 0^\circ$ and $\delta = 90^\circ$, which are the representative of a hypothesis testing problem with a prospective target moving either perpendicular or parallel to the baseline, respectively.

The results of the CFAR analysis are presented in Fig. 3 for $\delta = 0^\circ$ and Fig. 4 for $\delta = 90^\circ$, where, for each detector, the actual P_{fa} is plotted versus the normalized Doppler frequency at the monostatic node. Notably, according to (2) and (3), when $\delta = 0^\circ$, the bistatic Doppler equals the monostatic Doppler. Conversely, when $\delta = 90^\circ$, the bistatic Doppler is equal to 0. Subplots in Figs. 3 and 4 correspond to the different sea clutter datasets described in Table I. Specifically, they are organized as subfigures in a way that each row corresponds to a different bistatic angle, while the columns refer to the monostatic node operating in HH (left) and VH (right) polarization, respectively.

Overall, for the case $\delta = 0^\circ$ (i.e., Fig. 3), the P_{fa} curves exhibit a fairly constant behavior across all Doppler values, with slight mismatches, indicating that the system demonstrates a robust rather than strictly CFAR behavior. Furthermore, it is evident that all the considered polarimetric receivers share this behavior, with slight variations depending on the analyzed case. A deeper analysis reveals that for all VH datasets (right subplots of Fig. 3), the pol-HO receiver exhibits the poorest CFAR performance, with the actual P_{fa} slightly greater than its nominal value. These results provide further evidence on the influence of clutter diversity on the validity of some modeling assumptions. As a matter of fact, the hypothesis of equality between the clutter covariance matrices observed at the two bistatic nodes is generally valid only for a limited portion of the entire clutter dataset.

Noteworthy, in the case where the angle δ equals 90° (see Fig. 4), all receivers exhibit an approximately constant P_{fa} across the entire Doppler frequency range. Nonetheless, even under this configuration, the pol-HO and pol-PH receivers continue to yield the poorest performance, with effective P_{fa} values almost always exceeding the nominal ones. Furthermore, for all the tested datasets, at Doppler frequencies far from the sea-clutter spectra, and assuming a target movement parallel to the baseline, i.e., $\delta = 90^\circ$ (see Fig. 4), both the pol-HO and pol-PH receivers show poorer CFAR capabilities than the situation of a perpendicular trajectory $\delta = 0^\circ$ (see Fig. 3). This trend would suggest that the two bistatic receivers effectively experience a diverse covariance matrix with a more marked effect in the second scenario. It is also worth observing that in Fig. 4(c), the observed P_{fa} of all four detectors exceeds the nominal value likely due to nonnegligible mismatches between design assumptions (namely, Gaussian/SIRP disturbance and independent identically distributed secondary data) and actual conditions which can magnify false alarms especially in the clutter Doppler region. Nevertheless, despite these discrepancies, the results confirm that all detectors exhibit a robust CFAR behavior, maintaining a relatively stable false alarm rate across varying conditions.

In summary, all the considerations drawn for the scenario with $\delta = 0^\circ$ remain valid for $\delta = 90^\circ$. However, in this last configuration, both the pol-HO and pol-PH detectors tend to exhibit a generally higher P_{fa} value than the former case. This is not surprising since, according to the results of [33], vertical polarization at the transmitter tends to result in stronger sea clutter returns in both the cross-polarized bistatic channels than the horizontal polarization. This leads to higher clutter power, which can negatively affect the CFAR performance. This trend is in line with empirical observations reported in prior studies on monostatic and multistatic sea-clutter environments [8], [33], and it reflects intrinsic properties of sea-surface scattering mechanisms at low grazing angles. Notably, the pol-HE detector continues to represent the most reliable option in terms of CFAR behavior.

To aid in the visualization of the CFAR analysis results, Table II summarizes the normalized average deviation of the empirical CFAR from the theoretical P_{fa} for each detector considered.

C. Detection Performance

In this section, the detection performance of the designed architectures is evaluated by synthetically injecting into the available clutter data, a target representative of a small boat, whose RCS (monostatic and bistatic-polarimetric) has been synthesized leveraging the MATLAB POFacets toolbox [44], [45]. Specifically, a target with length, width, and height equal to 2.20 m × 1.47 m × 0.78 m, respectively, and made of E-glass (electrical glass, a material widely used in the fabrication of small boats), is modeled as an array of triangular-shaped elements (facets), as shown in Fig. 5(a). To evaluate both the monostatic and bistatic (co-polarized) RCSs of the target, POFacets computes the square modulus of the scattered field (obtained as the superposition of contributions from individual facets) and divides it by the square modulus of the incident field. Accordingly, the RCS data have been obtained using the same parameters as those of the NetRAD system, with the transmit polarization and bistatic angles matching those of the datasets exploited for the present analysis.

The simulations have been carried out according to the basic scheme, as illustrated in Fig. 6. Going further into detail, it is assumed that the target lies in the same horizontal plane as the radar (i.e., elevation differences are not considered). Once the transmitter's pointing direction is fixed, the target's response depends on its actual orientation (aspect angle) with respect to the transmitter and receiver. To formally describe the sensing scenario, let us introduce a local coordinate system centered on the target, so as to describe the possible rotations of the target with respect to the reference x-axis via the angle ϕ_T [see Fig. 5(b)]. The same angle ϕ_T also characterizes the target scattering properties

---

[3] Notice that the chosen P_{fa} value is essentially dictated by the limited amount of available measured data.

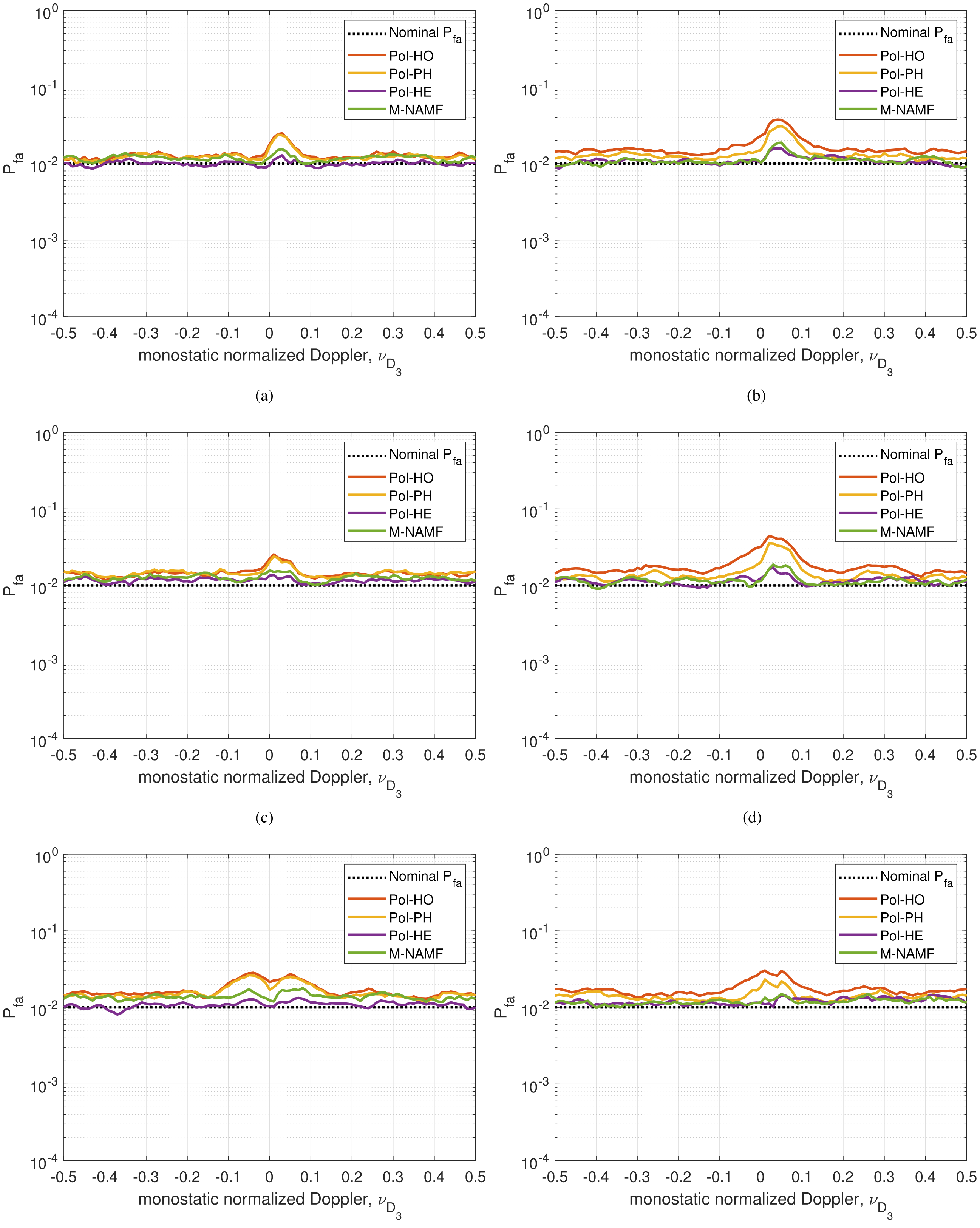

(a) (b) (c) (d) (e) (f)

Fig. 3. Actual P_{fa} versus ν_{D_3}, setting $\delta = 0^\circ$, $N = 8$, $K = 16$, and a nominal $P_{\text{fa}} = 10^{-2}$. Subplots refer to the NetRAD dataset. (a) 1. (b) 8. (c) 4. (d) 11. (e) 5. (f) 12. (a) Dataset 1 ($\beta = 60^\circ$, H-pol in Tx). (b) Dataset 8 ($\beta = 60^\circ$, V-pol in Tx). (c) Dataset 4 ($\beta = 90^\circ$, H-pol in Tx). (d) Dataset 11 ($\beta = 90^\circ$, V-pol in Tx). (e) Dataset 5 ($\beta = 120^\circ$, H-pol in Tx). (f) Dataset 12 ($\beta = 120^\circ$, V-pol in Tx).

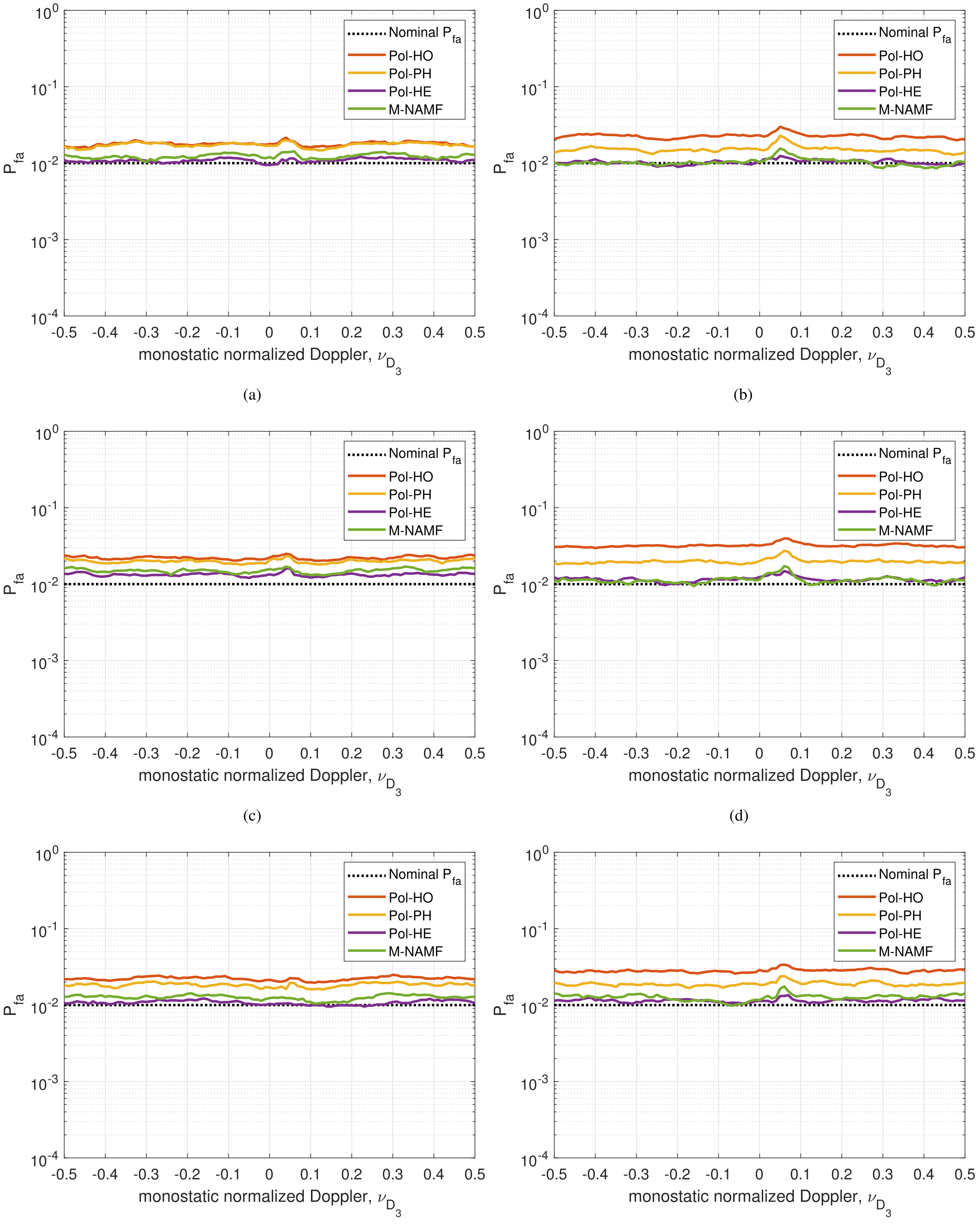

(a)

(b)

(c)

(d)

(e)

(f)

Fig. 4. Actual P_{fa} versus ν_{D_3}, setting $\delta = 90^\circ$, $N = 8$, $K = 16$, and a nominal $P_{fa} = 10^{-2}$. Subplots refer to the NetRAD dataset. (a) 1. (b) 8. (c) 4. (d) 11. (e) 5. (f) 12. (a) Dataset 1 ($\beta = 60^\circ$, H-pol in Tx). (b) Dataset 8 ($\beta = 60^\circ$, V-pol in Tx). (c) Dataset 4 ($\beta = 90^\circ$, H-pol in Tx). (d) Dataset 11 ($\beta = 90^\circ$, V-pol in Tx). (e) Dataset 5 ($\beta = 120^\circ$, H-pol in Tx). (f) Dataset 12 ($\beta = 120^\circ$, V-pol in Tx).

TABLE II
Average CFAR Deviation From the Theoretical P_{fa} Normalized to Its Nominal Value (i.e., 10^{-2}) for the Scenario With $N = 8$, $K = 16$, and $\delta \in \{0^\circ, 90^\circ\}$

Datasets	**pol-HO**		**pol-PH**		**pol-HE**		**M-NAMF**	
	$\delta = 0^\circ$	$\delta = 90^\circ$	$\delta = 0^\circ$	$\delta = 90^\circ$	$\delta = 0^\circ$	$\delta = 90^\circ$	$\delta = 0^\circ$	$\delta = 90^\circ$
1	0.31	0.79	0.25	0.72	0.06	0.09	0.18	0.23
4	0.47	1.21	0.48	0.99	0.17	0.33	0.27	0.50
5	0.70	1.22	0.62	0.85	0.11	0.08	0.39	0.27
8	0.66	1.27	0.36	0.51	0.11	0.06	0.13	0.08
11	0.88	2.21	0.48	0.99	0.16	0.16	0.17	0.14
12	0.75	1.82	0.42	0.90	0.20	0.15	0.19	0.27

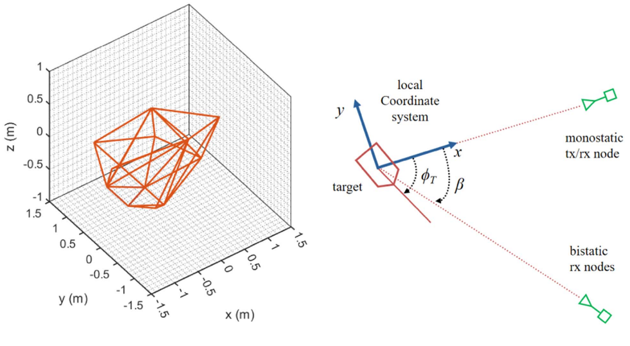

(a) (b)

Fig. 5. POFacets model of a small boat made of E-glass material with length, width, and height equal to 2.20 m × 1.47 m × 0.78 m, respectively. Its RCS is evaluated both in the monostatic and bistatic (co-polarized) configurations. (a) PoFacets model. (b) Reference system.

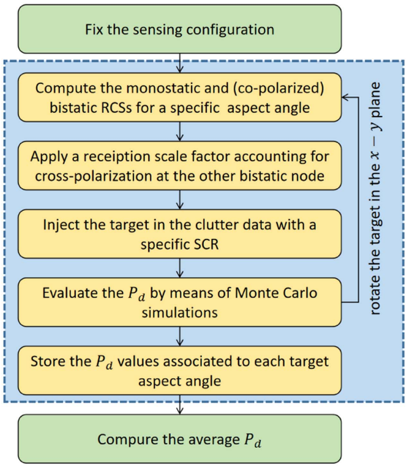

Fig. 6. Flowchart illustrating the simulation process used to evaluate the P_d.

for the bistatic nodes (for fixed sensing configuration, i.e., angle β).

Thus, ϕ_T is discretized within the interval $[0^\circ, 360^\circ)$, in steps of 10°, resulting in a total of $D = 36$ discrete measurements. Specifically, for each target aspect angle $\phi_T^{(h)} \in \{0^\circ, 10^\circ, \ldots, 350^\circ\}$, $h = 1, \ldots, D$, both monostatic and (copolarized) bistatic RCSs are computed, viz., $\sigma_m^{(h)}$ and $\sigma_b^{(h)}$, $h = 1, \ldots, D$.

The actual $P_d^{(h)}$ is evaluated for each pair of monostatic and bistatic target RCSs ($\sigma_m^{(h)}$ and $\sigma_b^{(h)}$, respectively), $h = 1, \ldots, D$. It is estimated as the number of times the test statistic exceeds the corresponding threshold, which is determined, for each detector, using clutter data free of target components to ensure a nominal[4] $P_{\text{fa}} = 10^{-2}$. The target (entirely contained in a resolution cell) is modeled as a point-like moving scatterer with a specified signal-to-clutter ratio (SCR) and velocity. For the multistatic system, the global SCR is the sum of all the local SCR_i, $i = 1, \ldots, 3$

$$\text{SCR} = \sum_{i=1}^{3} \text{SCR}_i$$

where the local integrated SCR at the monostatic node is given by

$$\text{SCR}_3 = |\bar{\alpha}_3^{\text{rms}}|^2 \boldsymbol{s}_3^\dagger \boldsymbol{M}_3^{-1} \boldsymbol{s}_3.$$

The scattering parameters that determine the complex amplitude of the echo at each receiving sensor are fixed to ensure a given integrated SCR at the monostatic node, namely

$$\alpha_3^{(h)} = \bar{\alpha}_3^{\text{rms}} \sqrt{\overline{\sigma}_m^{(h)}} e^{j\varphi_3^{(h)}}, \quad h = 1, \ldots, D \tag{18}$$

where $\varphi_3^{(h)} \sim \mathcal{U}[0, 2\pi]$, and

$$\bar{\alpha}_3^{\text{rms}} = \sqrt{\frac{\text{SCR}_3}{\boldsymbol{s}_3^\dagger \boldsymbol{M}_3^{-1} \boldsymbol{s}_3}}. \tag{19}$$

In (18), $\boldsymbol{M}_3$ is estimated by means of $\bar{\boldsymbol{R}}_3$, that is, the overall SCM computed from the clutter data at the monostatic sensor, whereas $\overline{\sigma}_m^{(h)}$ is the monostatic RCS at the aspect angle ϕ_h, $h = 1, \ldots, D$, normalized to its mean value computed over all the available aspect angles, i.e.,

$$\overline{\sigma}_m^{(h)} = \frac{\sigma_m^{(h)}}{\sigma_m^c}, \quad h = 1, \ldots, D \tag{20}$$

with $\sigma_m^c = \frac{1}{D}\sum_{h=1}^{D} \sigma_m^{(h)}$ denoting the sample mean of the monostatic RCS data.

Hence, assuming the transmission with polarization H, once the monostatic amplitude of the target, $\alpha_3^{(h)}$, $h = 1, \ldots, D$, is set to achieve the desired SCR_3, the bistatic

---

[4] Note that the thresholds are set directly from measured data so as to ensure the same actual P_{fa} for all the receivers (the same empirical number of false alarms are forced).

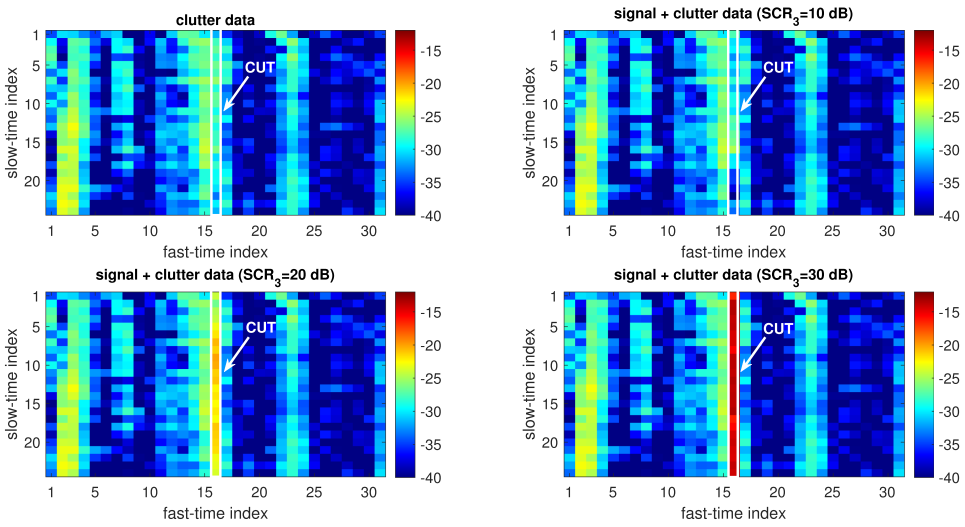

Fig. 7. Modulus of the radar data (expressed in dB) for different values of SCR$_3$. A synthetic target, representative of a small boat, is injected in the clutter data (NetRAD dataset number 1) with $v_0 = 5$ m/s, $\delta = 0^\circ$, $N = 8$, and $K = 16$.

amplitudes at the other two nodes are set as follows:

$$\alpha_1^{(h)} = \bar{\alpha}_3^{\text{rms}} \sqrt{\frac{\sigma_b^{(h)}}{\sigma_m^c}} e^{j\varphi_1^{(h)}}, \quad h = 1, \dots, D$$
$$\alpha_2^{(h)} = \bar{\alpha}_3^{\text{rms}} \sqrt{\frac{\sigma_b^{(h)}}{\sigma_m^c}} \sqrt{\epsilon_2} e^{j\varphi_2^{(h)}}, \quad h = 1, \dots, D \tag{21}$$

where $\sigma_b^{(h)}$ is the bistatic RCS obtained directly as output from the POFacets simulator, and $\{\varphi_1^{(h)}, \varphi_2^{(h)}\} \sim \mathcal{U}[0, 2\pi]$, with $\varphi_l^{(h)}, l = 1, \dots, 3, h = 1, \dots, D$, statistically independent. The term ϵ_2 represents the possible RCS reduction due to cross-polarization effects at the bistatic receiver [56], and is, herein, set to 0.19 [57]. When the transmitting polarization is V, the roles of nodes 1 and 2 are reversed.

To assess the impact of sea clutter on detection performance, the target Doppler frequency is limited to the clutter dominated region for both monostatic and bistatic configurations [34]. Hence, a target with a velocity of $v_0 = 5$ m/s is assumed, and the following two different velocity directions are considered.

1) Orthogonally to the baseline ($\delta = 0^\circ$).
2) Parallel to the baseline ($\delta = 90^\circ$).

In both cases, the resulting Doppler frequencies are computed according to (2) and (3) for the bistatic and monostatic nodes, respectively.

To help readers in understanding the resulting signal characteristics, Fig. 7 illustrates the modulus of the fast-time/slow-time data (expressed in dB) at the monostatic node for different values of SCR$_3$. The figures refer to the scenario with a synthetic target injected in the NetRAD clutter (dataset 1) with $v_0 = 5$ m/s, $\delta = 0^\circ$, $N = 8$, and $K = 16$, with the CUT highlighted by the white rectangle. This visualization is intended to provide a clearer representation of how the injected target appears within the clutter background under varying SCR ratios.

With the above settings in mind, once the $P_d^{(h)}$ curves, $h = 1, \dots, D$, are available for each target aspect angle, the average P_d (with respect to the target aspect angle) versus SCR$_3$ is calculated and used as the final performance metric for each detector, i.e.,

$$P_d = \frac{1}{D} \sum_{h=1}^{D} P_d^{(h)}. \tag{22}$$

Results are presented in Figs. 8 and 9, corresponding to scenarios with $\delta = 0^\circ$ and $\delta = 90^\circ$, respectively. The plots illustrate the average P_d versus SCR$_3$ (expressed in dB). Both figures refer to the previously described scenario with $N = 8$ and $K = 16$ secondary data samples used for covariance estimation. In addition, the different subplots correspond to the NetRAD datasets are listed in Table I.

The average P_d curves clearly show that the pol-HE receiver outperforms the counterparts regardless of the dataset (i.e., polarization configuration, bistatic angle, and target motion direction). Furthermore, the pol-HO and pol-PH receivers exhibit comparable performance, with the pol-PH providing marginal improvements over the pol-HO. Similarly, the M-NAMF receiver generally reaches performance levels close to those of the pol-PH. In contrast, the m-NAMF yields the lowest performance, with a significant degradation relative to all other receivers considered in this study.[5] As an illustrative example, the m-NAMF needs roughly 15 dB extra SCR$_3$ than the other receivers to reach P_d of 0.6. The reason for this behavior is primarily due to the fact that it employs only a single receiver, and therefore does not take advantage of either the polarization or the spatial diversity offered by the multistatic/polarimetric network.

---

[5] Additional comparisons, not reported to avoid plot overcrowding, have highlighted that Kelly and adaptive coherence estimator (ACE) detectors exhibit a performance comparable to the m-NAMF and are significantly outperformed by the devised detectors.

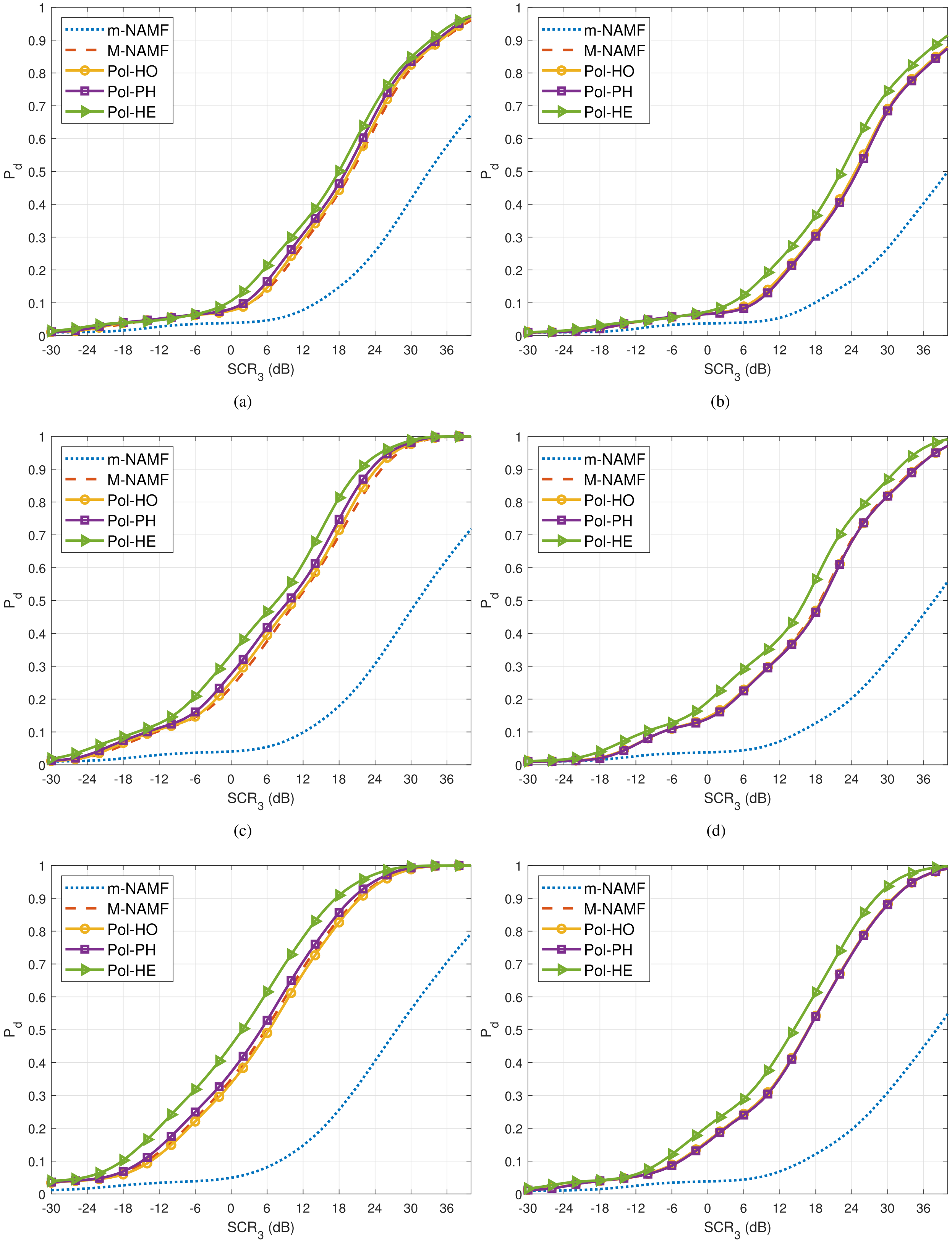

(a)

(b)

(c)

(d)

(e)

(f)

Fig. 8. Average P_d versus SCR$_3$ (expressed in dB). Tests are conducted with the following parameters setting: $N = 8$, $K = 16$, and nominal $P_{\mathrm{fa}} = 10^{-2}$. Moreover, a synthetic target, representative of a small boat, is injected in the clutter data with $v_0 = 5$ m/s and $\delta = 0°$. The NetRAD dataset. (a) 1. (b) 8. (c) 4. (d) 11. (e) 5. (f) 12. (a) Dataset 1 ($\beta = 60°$, H-pol in Tx). (b) Dataset 8 ($\beta = 60°$, V-pol in Tx). (c) Dataset 4 ($\beta = 90°$, H-pol in Tx). (d) Dataset 11 ($\beta = 90°$, V-pol in Tx). (e) Dataset 5 ($\beta = 120°$, H-pol in Tx). (f) Dataset 12 ($\beta = 120°$, V-pol in Tx).

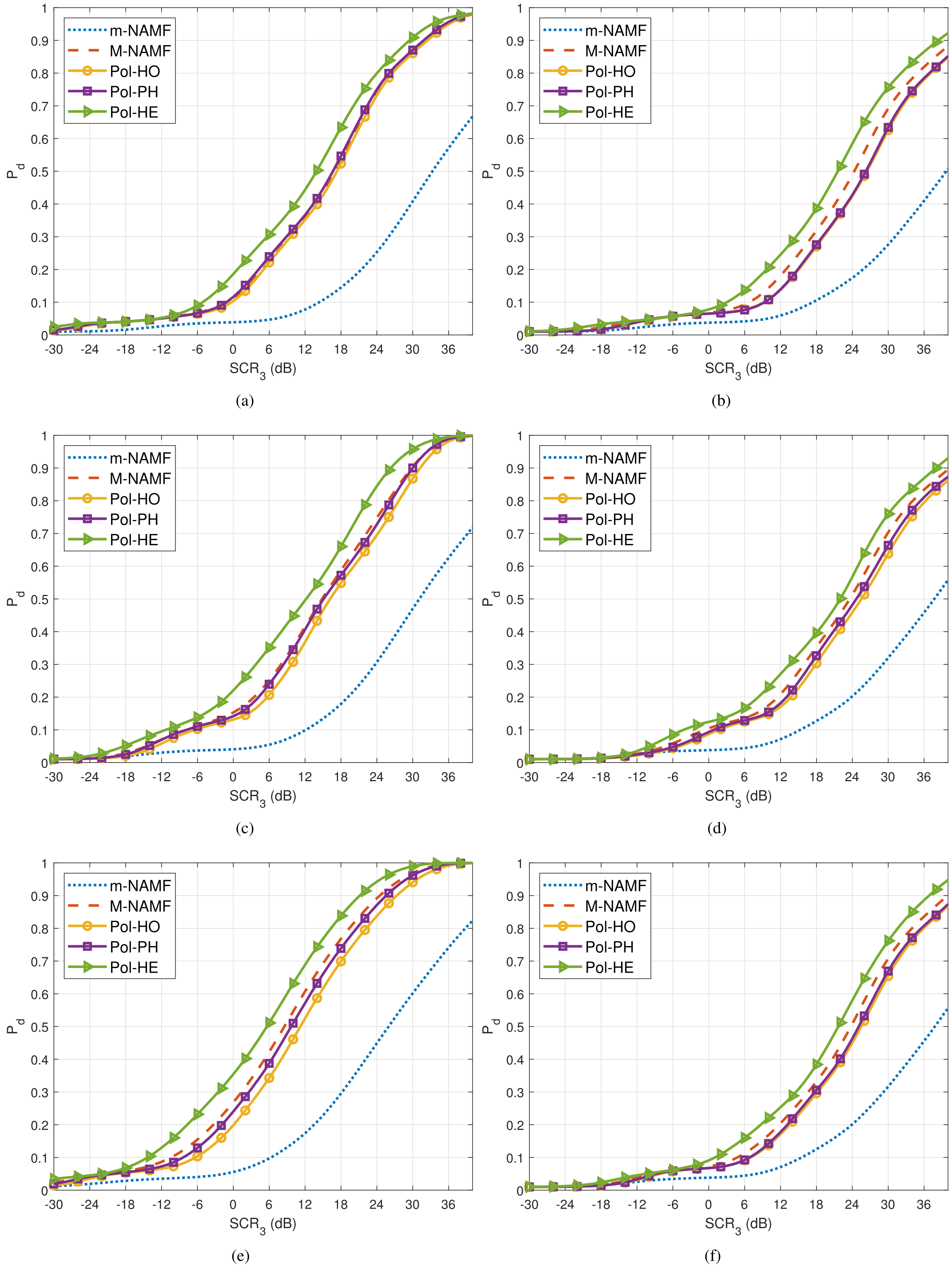

(a) (b)

(c) (d)

(e) (f)

Fig. 9. Average P_d versus SCR$_3$ (expressed in dB). Tests are conducted with the following parameters setting: $N = 8$, $K = 16$, and nominal $P_{fa} = 10^{-2}$. Moreover, a synthetic target, representative of a small boat, is injected in the clutter data with $v_0 = 5$ m/s and $\delta = 90^\circ$. Tthe NetRAD dataset. (a) 1. (b) 8. (c) 4. (d) 11. (e) 5. (f) 12. (a) Dataset 1 ($\beta = 60^\circ$, H-pol in Tx). (b) Dataset 8 ($\beta = 60^\circ$, V-pol in Tx). (c) Dataset 4 ($\beta = 90^\circ$, H-pol in Tx). (d) Dataset 11 ($\beta = 90^\circ$, V-pol in Tx). (e) Dataset 5 ($\beta = 120^\circ$, H-pol in Tx). (f) Dataset 12 ($\beta = 120^\circ$, V-pol in Tx).

Notably, horizontal polarization in transmission leads to better P_d performance. Moreover, increasing the angle δ from 0° to 90° magnifies the differences among the curves, with the pol-HE receiver showing the greatest performance improvement. Another interesting case is illustrated in Fig. 9(b), (d), and (f), where the target moves parallel to the baseline and the vertical polarization is used for transmission. In this configuration, the pol-HE receiver

TABLE III

P_d Gain of the pol-HE Algorithm With Respect to the Other Detectors, for the Scenario With $N = 8$, $K = 16$, and $\delta \in \{0^\circ, 90^\circ\}$

Dataset	**M-NAMF**		**pol-HO**		**pol-PH**		**m-NAMF**	
	$\delta = 0^\circ$	$\delta = 90^\circ$	$\delta = 0^\circ$	$\delta = 90^\circ$	$\delta = 0^\circ$	$\delta = 90^\circ$	$\delta = 0^\circ$	$\delta = 90^\circ$
1	0.07	0.09	0.06	0.10	0.04	0.08	0.39	0.52
4	0.11	0.08	0.08	0.13	0.05	0.10	0.65	0.51
5	0.06	0.07	0.07	0.13	0.04	0.09	0.63	0.53
8	0.07	0.08	0.07	0.13	0.07	0.12	0.30	0.32
11	0.09	0.04	0.10	0.09	0.10	0.06	0.49	0.30
12	0.07	0.06	0.07	0.10	0.07	0.10	0.53	0.30

The gains are computed at SCR = 25 dB.

continues to achieve the best performance, whereas the pol-PH architecture shows a reduction in P_d values, dropping below those of the M-NAMF. This can be explained by noting that while some portions of the entire data show structured covariance matrices, this is not true for the majority of the dataset. In fact, the amount of structured data is relatively small according to the findings presented in [34]. As a result, the overall analysis, which averages over all data, tends to favor the HE receiver, as it does not rely on such structures and is more suited to general conditions, due to its intrinsic robustness. However, when the data have a more persistent structure, the other receivers will likely perform better than the HE counterpart. Furthermore, the P_d curves, as shown in Fig. 9, achieves smaller values than those of Fig. 8, also due to the stronger sea clutter returns caused by the use of vertical polarization at the transmitter, as already observed in the CFAR analyses.

To facilitate the performance comparison, Table III reports the P_d gain of the pol-HE algorithm over its competitors for a fixed SCR of 25 dB. The results refer to the case with $N = 8$, $K = 16$, and both $\delta = 0^\circ$ and $\delta = 90^\circ$.

Further analyses conducted with intermediate values of the parameter δ (e.g., 45°), not reported here for brevity, yield results consistent with the trends observed in the two limiting cases of $\delta = 0^\circ$ and 90°, further reinforcing the generality of the findings.

D. Sensitivity Analysis

This section is devoted to evaluating the influence of the setting parameters (viz., K, Q_1, and Q_2) on the performance of the proposed detectors. To this end, a sensitivity analysis is carried out, considering the following case studies.

1) $N = 8$ and $K = 12$ ($1.5N$).
2) $N = 8$ and $K = 16$ ($2N$).
3) $N = 8$ and $K = 20$ ($2.5N$).

The analysis is limited to the pol-HE detector, which demonstrated the best performance in terms of both CFAR and detection capability, as shown in the previous subsections. The focus is on datasets 1 and 8, corresponding to $\beta = 60^\circ$ with horizontal and vertical polarization at the monostatic node, respectively, and assuming $\delta = 0^\circ$. The results of this assessment are presented in Fig. 10.

The reported average P_d curves indicate the following.

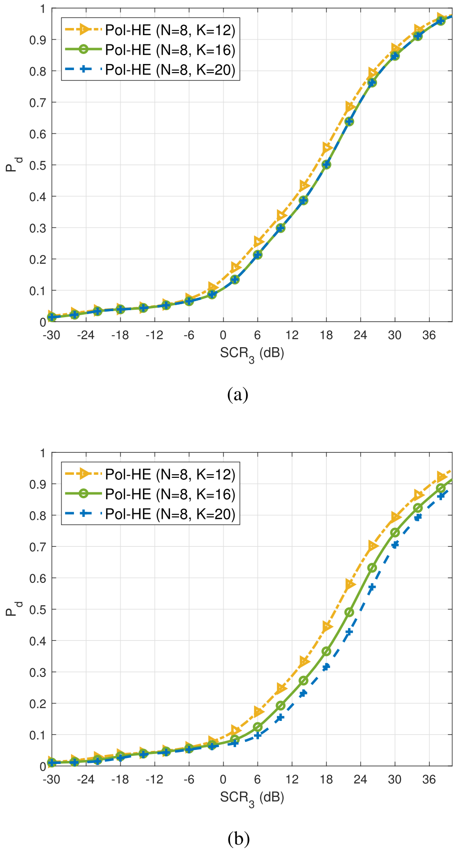

(a)

(b)

Fig. 10. Average P_d versus SCR_3 (expressed in dB) for the pol-HE detector for different values of K. A nominal $P_{\mathrm{fa}} = 10^{-2}$ is assumed, and a synthetic target, representative of a small boat, is injected in the clutter data with $v_0 = 5$ m/s and $\delta = 0^\circ$. The NetRAD dataset. (a) 1. (b) 8. (a) Dataset 1 ($\beta = 60^\circ$, H-pol in Tx). (b) Dataset 8 ($\beta = 60^\circ$, V-pol in Tx).

1) When horizontal polarization is used at the transmit side (dataset 1), the cases $K = 12$ and $K = 16$ provide the same performance.
2) When vertical polarization is used at the transmit side (dataset 8), the case $K = 12$ provides the best performance.
3) Regardless of the polarimetric setup, the case $K = 20$ yields the worst performance.

Apparently, these results seem to be in contrast with the theoretical expectations, according to which increasing

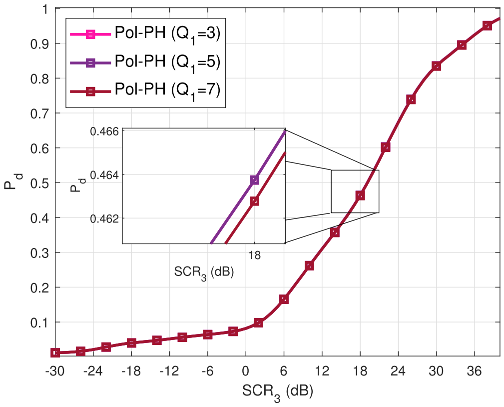

Fig. 11. Average P_d versus SCR_3 (expressed in dB) for the pol-PH receiver, and for varying Q_1. Tests are conducted with the following parameters setting: $N = 8$, $K = 16$, and nominal $P_{\mathrm{fa}} = 10^{-2}$. Moreover, a synthetic target, representative of a small boat, is injected in the clutter data (NetRAD dataset number 1) with $v_0 = 5$ m/s and $\delta = 0°$.

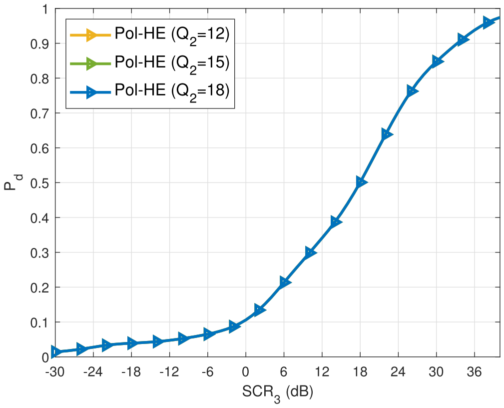

Fig. 12. Average P_d versus SCR_3 (expressed in dB) for the pol-HE receiver, and for varying Q_2. Tests are conducted with the following parameters setting: $N = 8$, $K = 16$, and nominal $P_{fa} = 10^{-2}$. Moreover, a synthetic target, representative of a small boat, is injected in the clutter data (NetRAD dataset number 1) with $v_0 = 5$ m/s and $\delta = 0°$.

K should lead to more reliable covariance matrix estimates and therefore better performance. However, from a practical point of view, this discrepancy can be explained by the fact that a larger number of secondary data may include range bins whose slow-time returns exhibit statistical properties different from those of the CUT, which can degrade the estimation quality and thus impair detection performance. This model mismatch, along with the observation that multistatic sea clutter tends to be more challenging to mitigate when vertical polarization is used to probe the environment, also provide plausible explanations for the behavior observed in dataset 8.

Regarding the number of iterations, the plots of Figs. 11 and 12 illustrate the average P_d versus SCR_3 for different values of Q_1 and Q_2. Therein, the previously described scenario with $N = 8, K = 16, \delta = 0°$, and NetRAD datasets number 1 is considered. As shown in Fig. 11 (for varying Q_1) and Fig. 12 (for varying Q_2), the detection performance curves computed with different values of Q_1 and Q_2 substantially overlap.

IV. CONCLUSION

This article presented three adaptive detection architectures for point-like targets in sea-clutter environments, designed for a multistatic polarimetric radar system consisting of one monostatic and two colocated, cross-polarized bistatic sensors. The proposed schemes exploit all radar returns while accounting for range-domain heterogeneity and relationships among statistical features of the bistatic clutter components. By incorporating structured estimates of nuisance parameters, the detectors were derived through a two-step GLRT framework, resulting in a robust and flexible approach to target detection in challenging radar network scenarios.

At the analysis stage, both the CFAR characteristics and detection performance were evaluated using sea-clutter data gathered with the NetRAD system across varying acquisition geometries and polarimetric conditions. The results showed that regardless of the sensing configuration, the pol-HE detector outperformed the competitors in terms of both CFAR stability and target detectability. In contrast, the pol-HO and pol-PH receivers exhibited some slight deviations from the nominal P_{fa}, highlighting a robust CFAR behavior. Moreover, the extent of deviations depends on the geometric and polarimetric setup, further confirming the impact of clutter diversity. In terms of detection probability, both pol-HO and pol-PH incurred moderate losses compared to the pol-HE, although their P_d curves closely followed those of the M-NAMF across most of the evaluated scenarios.

Future research efforts may focus on extending the analysis to additional multistatic and polarimetric datasets (network configurations). Moreover, a future study could involve a two-step approach in which an environment classifier would first learn and infer relationships between bistatic covariance matrices, to identify clutter homogeneity state. Then, a bespoke receiver (viz., pol-HE, pol-HO, or pol-PH) could be selected based on the classification output to optimize structure exploitation and potentially enhance the system performance. Finally, it would also be of interest to consider more complex covariance structures, see, e.g., [58].

ACKNOWLEDGMENT

The authors would like to thank Dr. F. Fioranelli and to the teams from University College London (UCL) and the University of Cape Town (UCT) for collecting the data and making them available for this analysis.The authors would also like to thank the EiC, AEiC, SE, AE, and the Referees for the careful review of the paper.

REFERENCES

[1] D. W. O'Hagan, S. R. Doughty, and M. R. Inggs, "Chapter 5-Multistatic radar systems," in *Academic Press Library in Signal Processing*, vol. 7, R. Chellappa and S. Theodoridis, Eds., Cambridge, MA, USA: Academic Press, 2018, pp. 253–275.

[2] H. D. Griffiths, “Keynote address: Clutter diversity: A new degree of freedom in multistatic radar,” in *Proc. 2014 IEEE Radar Conf.*, 2014, pp. 11–11.

[3] R. Klemm, U. Nickel, C. Gierull, P. Lombardo, H. Griffiths, and W. Koch, *Novel Radar Techniques and Applications Volume 2: Waveform Diversity and Cognitive Radar, and Target Tracking and Data Fusion, Ser. Radar, Sonar & Navigation*. London, U.K.: Inst. Eng. Technol., 2017.

[4] S. Bocquet, “Suzuki distributed monostatic and bistatic S-band radar sea clutter,” *IEEE Trans. Aerosp. Electron. Syst.*, vol. 59, no. 1, pp. 650–659, Feb. 2023.

[5] V. Carotenuto, A. Aubry, A. De Maio, and F. Fioranelli, “Multivariate polarimetric bistatic clutter statistical analysis,” in *Proc. 2022 IEEE Radar Conf.*, 2022, pp. 1–6.

[6] M. A. Richards, J. A. Scheer, and W. A. Holm, Eds., *Principles of Modern Radar: Basic Principles, Ser. Radar, Sonar & Navigation*. London, U.K.: Inst. Eng. Technol., 2010.

[7] A. Aubry, A. De Maio, and A. Farina, Eds., *Polarimetric Radar Signal Processing, Ser. Radar, Sonar and Navigation*. Stevenage, England: Inst. Eng. Technol., Feb. 2023.

[8] L. Rosenberg and S. Watts, *Radar Sea Clutter: Modelling and Target Detection, Ser. IET Radar, Sonar & Navigation*. London, U.K.: Inst. Eng. Technol., 2021.

[9] H. Melief, H. Greidanus, P. van Genderen, and P. Hoogeboom, “Analysis of sea spikes in radar sea clutter data,” *IEEE Trans. Geosci. Remote Sens.*, vol. 44, no. 4, pp. 985–993, Apr. 2006.

[10] S. Bocquet, “Analysis and simulation of low grazing angle X-band coherent radar sea clutter using memoryless nonlinear transformations,” *IEEE Trans. Geosci. Remote Sens.*, vol. 60, 2022, Art. no. 5111113.

[11] L. Rosenberg, “Parametric modeling of sea clutter Doppler spectra,” *IEEE Trans. Geosci. Remote Sens.*, vol. 60, 2022, Art. no. 5105409.

[12] J. Carretero-Moya, J. Gismero-Menoyo, A. Blanco-del Campo, and A. Asensio-Lopez, “Statistical analysis of a high-resolution sea-clutter database,” *IEEE Trans. Geosci. Remote Sens.*, vol. 48, no. 4, pp. 2024–2037, Apr. 2010.

[13] J. Carretero-Moya, J. Gismero-Menoyo, A. Asensio-Lopez, and A. Blanco-Del-Campo, “Small-target detection in high-resolution heterogeneous sea-clutter: An empirical analysis,” *IEEE Trans. Aerosp. Electron. Syst.*, vol. 47, no. 3, pp. 1880–1898, Jul. 2011.

[14] G. Cui, N. Li, L. Pallotta, G. Foglia, and L. Kong, “Geometric barycenters for covariance estimation in compound-Gaussian clutter,” *IET Radar, Sonar Navigation*, vol. 11, no. 3, pp. 404–409, 2017.

[15] W. Al-Ashwal, “Measurement and modelling of bistatic sea clutter,” Ph.D. dissertation, Dept. Electron. Elect. Eng., Univ. College London, London, U.K., 2011.

[16] W. Al-Ashwal et al., “Statistical analysis of simultaneous monostatic and bistatic sea clutter at low grazing angles,” *Electron. Lett.*, vol. 47, pp. 621–622, May 2011.

[17] W. A. Al-Ashwal et al., “Measurements of bistatic radar sea clutter,” in *Proc. 2011 IEEE RadarCon*, 2011, pp. 217–221.

[18] H. Griffiths, “Developments in bistatic and networked radar,” in *Proc. 2011 IEEE CIE Int. Conf. Radar*, 2011, pp. 10–13.

[19] M. A. Ritchie, W. A. Al-Ashwal, A. G. Stove, K. Woodbridge, and H. D. Griffiths, “Statistical analysis of monostatic and bistatic sea clutter Doppler spectrum,” in *Proc. 2011 IEEE CIE Int. Conf. Radar*, 2011, pp. 816–820.

[20] M. A. Ritchie, W. A. Al-Ashwal, A. G. Stove, K. Woodbridge, and H. D. Griffiths, “Coherent analysis of horizontally-polarized monostatic and bistatic sea clutter,” in *Proc. IET Int. Conf. Radar Syst.*, 2012, pp. 1–5.

[21] R. Palamà, M. Greco, P. Stinco, and F. Gini, “Statistical analysis of NetRAD high resolution sea clutter,” in *Proc. 21st Eur. Signal Process. Conf.*, 2013, pp. 1–5.

[22] R. Palamà, M. Greco, P. Stinco, and F. Gini, “Analysis of sea spikes in NetRad clutter,” in *Proc. 11th Eur. Radar Conf.*, 2014, pp. 109–112.

[23] W. A. Al-Ashwal, K. Woodbridge, and H. D. Griffiths, “Analysis of bistatic sea clutter - Part I: Average reflectivity,” *IEEE Trans. Aerosp. Electron. Syst.*, vol. 50, no. 2, pp. 1283–1292, Apr. 2014.

[24] W. A. Al-Ashwal, K. Woodbridge, and H. D. Griffiths, “Analysis of bistatic sea clutter - Part II: Amplitude statistics,” *IEEE Trans. Aerosp. Electron. Syst.*, vol. 50, no. 2, pp. 1293–1303, Apr. 2014.

[25] R. Palamà, M. S. Greco, P. Stinco, and F. Gini, “Statistical analysis of bistatic and monostatic sea clutter,” *IEEE Trans. Aerosp. Electron. Syst.*, vol. 51, no. 4, pp. 3036–3054, Oct. 2015.

[26] M. Ritchie, A. Stove, K. Woodbridge, and H. Griffiths, “NetRAD: Monostatic and bistatic sea clutter texture and Doppler spectra characterization at S-band,” *IEEE Trans. Geosci. Remote Sens.*, vol. 54, no. 9, pp. 5533–5543, Sep. 2016.

[27] F. Fioranelli, M. Ritchie, H. Griffiths, S. Sandenbergh, and M. Inggs, “Analysis of polarimetric bistatic sea clutter using the NetRAD radar system,” *IET Radar, Sonar Navigation*, vol. 10, no. 8, pp. 1356–1366, 2016.

[28] R. Palamà, M. Greco, and F. Gini, “Multistatic CFAR detection in non-Gaussian clutter,” in *Proc. 2016 IEEE Radar Conf.*, 2016, pp. 1–6.

[29] R. Palamà, M. Greco, and F. Gini, “Multistatic adaptive CFAR detection in non-Gaussian clutter,” *EURASIP J. Adv. Signal Process.*, vol. 107, 2016, Art. no. 107.

[30] R. Palamà et al., “Correlation analysis of simultaneously collected bistatic and monostatic sea clutter,” in *Proc. 2017 IEEE Radar Conf.*, 2017, pp. 1466–1471.

[31] L. Rosenberg, S. Watts, and M. S. Greco, “Modeling the statistics of microwave radar sea clutter,” *IEEE Aerosp. Electron. Syst. Mag.*, vol. 34, no. 10, pp. 44–75, Oct. 2019.

[32] S. Angelliaume, L. Rosenberg, and M. Ritchie, “Analysis of bistatic radar sea clutter amplitude distributions at low grazing angles,” in *Proc. 2019 Int. Radar Conf.*, 2019, pp. 1–5.

[33] A. Aubry, V. Carotenuto, A. De Maio, and F. Fioranelli, “Compatibility assessment of multistatic/polarimetric clutter data with the SIRP model,” *IEEE Trans. Aerosp. Electron. Syst.*, vol. 59, no. 1, pp. 359–374, Feb. 2023.

[34] A. Aubry, V. Carotenuto, A. De Maio, and F. Fioranelli, “Testing stationarity and statistical independence of multistatic/polarimetric sea-clutter with application to NetRAD data,” *IEEE Trans. Geosci. Remote Sens.*, vol. 62, 2024, Art. no. 5103415.

[35] K. Yao, “A representation theorem and its applications to spherically-invariant random processes,” *IEEE Trans. Inf. Theory*, vol. 19, no. 5, pp. 600–608, Sep. 1973.

[36] E. Conte and M. Longo, “Characterisation of radar clutter as a spherically invariant random process,” *IEE Proc. F (Commun., Radar Signal Process.)*, vol. 134, pp. 191–197, Apr. 1987.

[37] K. Ward, “Compound representation of high resolution sea clutter,” *Electron. Lett.*, vol. 17, pp. 561–563, Aug. 1981.

[38] E. Conte, M. Longo, and M. Lops, “Modelling and simulation of non-Rayleigh radar clutter,” *IEE Proc. F (Radar Signal Process.)*, vol. 138, pp. 121–130, Apr. 1991.

[39] E. Conte, A. De Maio, and C. Galdi, “Statistical analysis of real clutter at different range resolutions,” *IEEE Trans. Aerosp. Electron. Syst.*, vol. 40, no. 3, pp. 903–918, Jul. 2004.

[40] K. Sangston and K. Gerlach, “Coherent detection of radar targets in a non-Gaussian background,” *IEEE Trans. Aerosp. Electron. Syst.*, vol. 30, no. 2, pp. 330–340, Apr. 1994.

[41] H. Song, Y. Sun, R. Wang, W. Fei, Y. Wang, and J. Wang, “Phase estimation of distributed scatterer for high resolution data stacks in nonurban areas,” in *Proc. 2016 IEEE Int. Geosci. Remote Sens. Symp.*, 2016, pp. 5967–5970.

[42] H. Song et al., “Statistically homogeneous pixel selection for small SAR data sets based on the similarity test of the covariance matrix,” *Remote Sens. Lett.*, vol. 8, no. 10, pp. 927–936, 2017.

[43] F. Robey, D. Fuhrmann, E. Kelly, and R. Nitzberg, “A CFAR adaptive matched filter detector,” *IEEE Trans. Aerosp. Electron. Syst.*, vol. 28, no. 1, pp. 208–216, Jan. 1992.

[44] F. Chatzigeorgiadis and D. C. Jenn, “A MATLAB physical-optics RCS prediction code,” *IEEE Antennas Propag. Mag.*, vol. 46, no. 4, pp. 137–139, 2004.

[45] D. C. Jenn, 2024, Pofacets. [Online]. Available: https://faculty.nps.edu/jenn/

[46] C. Y. Chong, F. Pascal, J.-P. Ovarlez, and M. Lesturgie, "MIMO radar detection in non-Gaussian and heterogeneous clutter," *IEEE J. Sel. Topics Signal Process.*, vol. 4, no. 1, pp. 115–126, Feb. 2010.

[47] L. Rosenberg and Y. Abramovich, "Multi-static target detection in K-distributed sea clutter and Gaussian noise," in *Proc. 2017 IEEE Radar Conf.*, 2017, pp. 0346–0351.

[48] R. Palamà, L. Rosenberg, and H. Griffiths, "Performance evaluation of two multistatic radar detectors on real and simulated sea-clutter data," in *Proc. 2018 Int. Conf. Radar*, 2018, pp. 1–6.

[49] N. J. Willis, *Bistatic Radar*, vol. 2, Raleigh, NC, USA: SciTech Publishing, 2005.

[50] E. Conte, A. De Maio, and G. Ricci, "Recursive estimation of the covariance matrix of a compound-Gaussian process and its application to adaptive CFAR detection," *IEEE Trans. Signal Process.*, vol. 50, no. 8, pp. 1908–1915, Aug. 2002.

[51] P. Huang, H. Yang, X.-G. Xia, Z. Zou, X. Liu, and G. Liao, "A novel sea clutter rejection algorithm for spaceborne multichannel radar systems," *IEEE Trans. Geosci. Remote Sens.*, vol. 60, 2022, Art. no. 5117422.

[52] S. Gogineni et al., "High fidelity RF clutter modeling and simulation," *IEEE Aerosp. Electron. Syst. Mag.*, vol. 37, no. 11, pp. 24–43, Nov. 2022.

[53] J. Guerci, J. Bergin, R. Guerci, M. Khanin, and M. Rangaswamy, "A new MIMO clutter model for cognitive radar," in *Proc. 2016 IEEE Radar Conf.*, 2016, pp. 1–6.

[54] K. P. Rajput, M. B. Shankar, K. V. Mishra, M. Rangaswamy, and B. Ottersten, "CoFAR clutter estimation using covariance-free Bayesian learning," *IEEE Trans. Aerosp. Electron. Syst.*, vol. 61, no. 1, pp. 296–313, Feb. 2025.

[55] H. Tabatabaei and C. D. Richmond, "Deterministic vs stochastic modeling of clutter for adaptive radar detection," in *Proc. 2025 IEEE Int. Radar Conf.*, 2025, pp. 1–6.

[56] L. Novak, M. Sechtin, and M. Cardullo, "Studies of target detection algorithms that use polarimetric radar data," *IEEE Trans. Aerosp. Electron. Syst.*, vol. 25, no. 2, pp. 150–165, Mar. 1989.

[57] A. De Maio and G. Ricci, "A polarimetric adaptive matched filter," *Signal Process.*, vol. 81, no. 12, pp. 2583–2589, 2001. [Online]. Available: https://www.sciencedirect.com/science/article/pii/S0165168401001505

[58] A. Aubry, P. Babu, A. De Maio, and M. Rosamilia, "Advanced methods for MLE of toeplitz structured covariance matrices with applications to radar problems," *IEEE Trans. Inf. Theory*, vol. 70, no. 12, pp. 9277–9292, Dec. 2024.

Augusto Aubry (Senior Member, IEEE) received the Dr. Eng. degree in telecommunication engineering (with honors) and the Ph.D. degree in electronic and telecommunication engineering from the University of Naples Federico II, Naples, Italy, in 2007 and 2011, respectively.

From February to April 2012, he was a Visiting Researcher with the Hong Kong Baptist University, Hong Kong. He is currently an Associate Professor with the University of Naples Federico II. His research interests include statistical signal processing and optimization theory, with emphasis on MIMO communications and radar signal processing.

Dr. Aubry was the recipient of the 2022 IEEE Fred Nathanson Memorial Award as the young (less than 40 years of age) AESS Radar Engineer 2022, with the following citation "For outstanding contributions to the application of modern optimization theory to radar waveform design and adaptive signal processing" and the corecipient of the 2013 Best Paper Award (entitled to B. Carlton) of the IEEE Transactions on Aerospace and Electronic Systems with the contribution "Knowledge-Aided (Potentially Cognitive) Transmit Signal and Receive Filter Design in Signal-Dependent Clutter."

Vincenzo Carotenuto (Senior Member, IEEE) received the Dr. Eng. degree in telecommunication engineering and the Ph.D. degree in electronic and telecommunication engineering from the University of Naples Federico II, Naples, Italy, in 2010 and 2015, respectively.

From September to December 2022, he was a Visiting Researcher with the Delft University of Technology, Delft, The Netherlands. He is currently an Assistant Professor with the University of Naples Federico II. His research interests include statistical signal processing and radar signal processing.

Dr. Carotenuto was the corecipient of the Best Radar Paper Award at the 2018 and 2023 IEEE International Workshop on Metrology for Aerospace for his contributions titled "Assessing Spectral Compatibility Between Radar and Communication Systems on Measured Data" and "Experimental Evaluation of Radar Waveforms for Spectral Coexistence using the PARSAX radar," respectively.

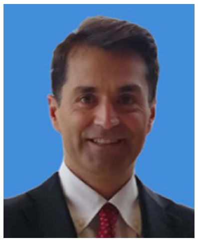

Antonio De Maio (Fellow, IEEE) received the Dr. Eng. (Hons.) and Ph.D. degrees in information engineering from the University of Naples Federico II, Naples, Italy, in 1998 and 2002, respectively.

From October to December 2004, he was a Visiting Researcher with the U.S. Air Force Research Laboratory, Rome, NY, USA. From November to December 2007, he was a Visiting Researcher with the Chinese University of Hong Kong, Hong Kong. He is currently a Professor with the University of Naples Federico II. His research interest lies in the field of statistical signal processing, radar detection, optimization theory applied to radar signal processing, and multiple-access communications.

Dr. De Maio was the recipient of the 2010 IEEE Fred Nathanson Memorial Award as the young (less than 40 years of age) AESS Radar Engineer 2010 whose performance is particularly noteworthy as evidenced by contributions to the radar art over a period of several years, with the following citation for "robust CFAR detection, knowledge-based radar signal processing, and waveform design and diversity" and the 2024 IEEE Warren White Award for outstanding achievements due to a major technical advance (or series of advances) in the art of radar engineering, with the citation "For Contributions to Radar Signal Processing Techniques for Target Detection, Waveform Design, and Electronic Protection." He was the corecipient of the 2013 best paper award (entitled to B. Carlton) of the IEEE Transactions on Aerospace and Electronic Systems with the contribution "Knowledge-Aided (Potentially Cognitive) Transmit Signal and Receive Filter Design in Signal-Dependent Clutter."

Luca Pallotta (Senior Member, IEEE) received the Laurea Specialistica degree (cum laude) in telecommunication engineering from the University of Sannio, Benevento, Italy, in 2009, and the Ph.D. degree in electronic and telecommunication engineering from the University of Naples Federico II, Naples, Italy, in 2014.

He is currently an Associate Professor with the University of Basilicata, Potenza, Italy. His research interest include the field of statistical signal processing, with emphasis on radar/SAR signal processing, radar targets detection and classification, and polarimetric radar/SAR.

Dr. Pallotta is an Associate Editor for IEEE JOURNAL OF SELECTED TOPICS IN APPLIED EARTH OBSERVATIONS AND REMOTE SENSING (JSTARS) since November 2020. From July 2018 to February 2021, he was an Associate Editor for the journal *Springer Signal, Image and Video Processing*. He was the recipient of the Student Paper Competition at the IEEE Radar Conference 2013.